Geophysical Journal International

Geophys. J. Int. (2016) **206,** 954–979
Advance Access publication 2016 April 29
GJI Seismology

doi: 10.1093/gji/ggw175

A seismic reference model for the crust and uppermost mantle beneath China from surface wave dispersion

Weisen Shen,[1] Michael H. Ritzwoller,[1] Dou Kang,[2] YoungHee Kim,[3] Fan-Chi Lin,[4] Jieyuan Ning,[2] Weitao Wang,[5] Yong Zheng[6] and Longquan Zhou[7]

[1] *Department of Physics, University of Colorado at Boulder, Boulder, CO* 80309*, USA. E-mail: weisen.shen@levee.wustl.edu*
[2] *Institute of Theoretical and Applied Geophysics, School of Earth and Space Sciences, Peking University, Beijing* 100871*, China*
[3] *School of Earth and Environmental Sciences, Seoul National University, Seoul* 151-742*, South Korea*
[4] *Department of Geology and Geophysics, University of Utah, Salt Lake City, UT* 84112-0102*, USA*
[5] *Institute of Geophysics, Chinese Earthquake Administration, Beijing* 100045*, China*
[6] *State Key Laboratory of Geodesy and Earth's Dynamics, Institute of Geodesy and Geophysics, Chinese Academy of Science, Wuhan* 43077*, China*
[7] *Chinese Earthquake Network Center, Chinese Earthquake Administration, Beijing* 100045*, China*

Accepted 2016 April 26. Received 2016 April 25; in original form 2015 May 2

SUMMARY

Using data from more than 2000 seismic stations from multiple networks arrayed throughout China (CEArray, China Array, NECESS, PASSCAL, GSN) and surrounding regions (Korean Seismic Network, F-Net, KNET), we perform ambient noise Rayleigh wave tomography across the entire region and earthquake tomography across parts of South China and Northeast China. We produce isotropic Rayleigh wave group and phase speed maps with uncertainty estimates from 8 to 50 s period across the entire region of study, and extend them to 70 s period where earthquake tomography is performed. Maps of azimuthal anisotropy are estimated simultaneously to minimize anisotropic bias in the isotropic maps, but are not discussed here. The 3D model is produced using a Bayesian Monte Carlo formalism covering all of China, extending eastwards through the Korean Peninsula, into the marginal seas, to Japan. We define the final model as the mean and standard deviation of the posterior distribution at each location on a $0.5^\circ \times 0.5^\circ$ grid from the surface to 150 km depth. Surface wave dispersion data do not strongly constrain internal interfaces, but shear wave speeds between the discontinuities in the crystalline crust and uppermost mantle are well determined. We design the resulting model as a reference model, which is intended to be useful to other researchers as a starting model, to predict seismic wave fields and observables and to predict other types of data (e.g. topography, gravity). The model and the data on which it is based are available for download. In addition, the model displays a great variety and considerable richness of geological and tectonic features in the crust and in the uppermost mantle deserving of further focus and continued interpretation.

Key words: Surface waves and free oscillations; Seismic tomography; Crustal structure; Asia.

1 INTRODUCTION

The purpose of this study is to present a reference seismic model of the crust and uppermost mantle to a depth of about 150 km beneath China and surrounding areas, notably Tibet, and also the Korean Peninsula, the Sea of Japan and the Yellow Sea. The model is based predominantly on Rayleigh wave group and phase speed curves derived from ambient noise at periods from 8 to 50 s, but the data set is augmented with Rayleigh wave phase speeds up to 70 s period in South China and parts of Northeast China. We generate the model by a Bayesian Monte Carlo inversion so that model uncertainties are determined in all variables. Ultimately, the model is designed to be used as a starting point for regional scale studies and future inversions that assimilate different kinds of data, as a basis for source location and characterization, and to predict other types of geophysical data (body wave traveltimes, surface wave propagation characteristics, gravity, temperatures, etc.).

This paper is a continuation and culmination of three earlier studies performed, respectively, in Tibet (Yang *et al.* 2010, 2012), South China (Zhou *et al.* 2012) and North and Northeast China (Zheng *et al.* 2011). The Rayleigh wave phase and group velocity data sets developed in these studies derived principally from the China Earthquake Array (CEArray) and PASSCAL installations in Tibet, but also included data from F-Net stations in Japan. They

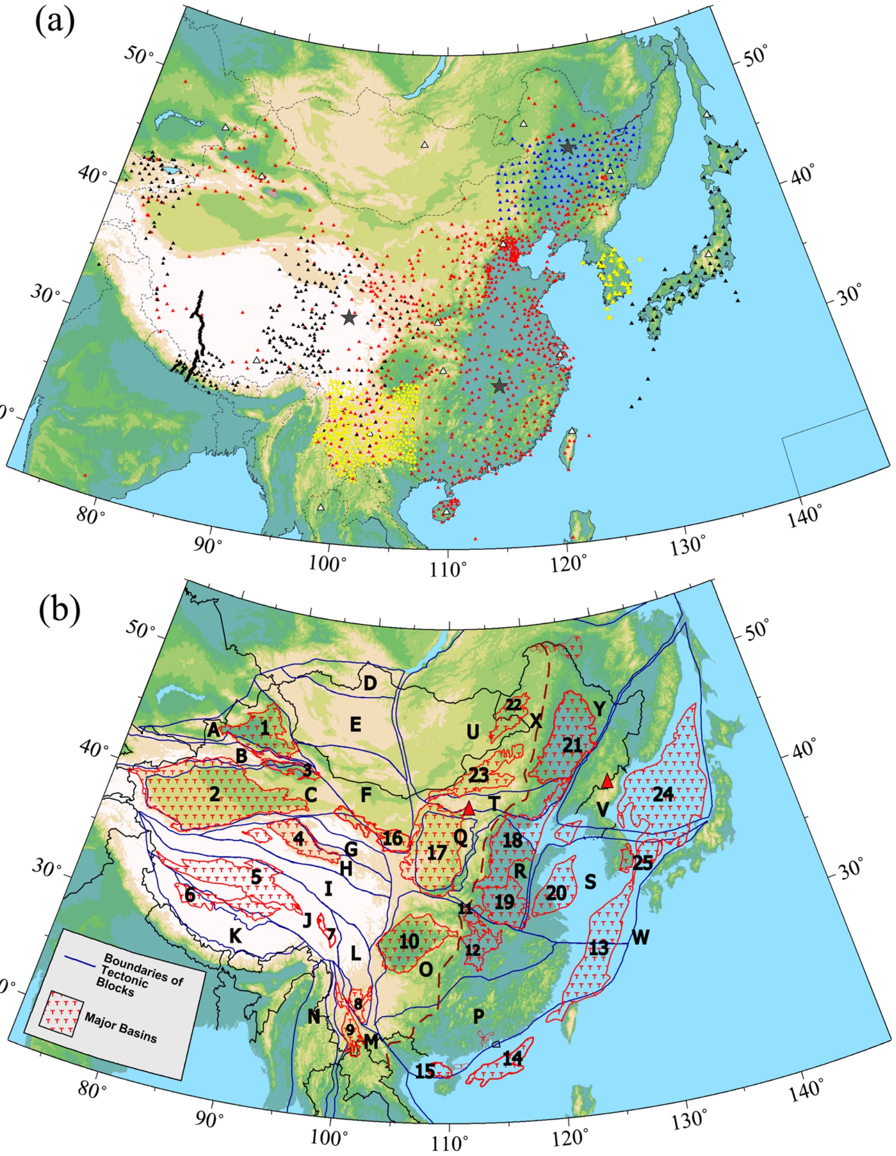

Figure 1. (a) Locations of the 2073 stations used in the current study—black triangles: PASSCAL stations, KNET stations or F-Net stations in Japan; red triangles: CEArray stations; yellow triangles: China Array or Korean National Seismic Network stations; blue triangles: NECESS array stations; white triangles: GSN or CDSN stations. The grey stars identify the three locations where we present data (Fig. 7), prior and posterior distributions (Figs 14–16), and model envelopes (Fig. 17). (b) Tectonic features and major basins identified in Table 1. The north–south directed dashed line is the North–South Gravity Lineament and the large red triangles are the locations of Datong and Changbaishan volcanoes.

were based primarily on ambient noise measurements, although Zhou *et al.* (2012) also developed an earthquake-derived data set for South China. The regions of these studies overlapped somewhat near their boundaries and there was some redundancy between the data sets. We assimilate the data sets produced in these studies here, but because these data sets are confined to particular sub-regions of China, the tomographic maps and models derived from them degrade near the boundaries of each region. Moreover, we have attempted to estimate uncertainties in the surface wave dispersion maps more rigorously than the earlier studies, consistent with the intent that our model will be a reference model. In addition, we augment the data used in the earlier studies by introducing new data from the NECESS (Northeast China Extended Seismic Network) array, the Korean Seismic Network, the China Array centred on Yunnan Province near the southeastern Tibetan Plateau and south of the Sichuan Basin, and, importantly, new measurements between the three regions based on CEArray stations, which effectively knits together these separate regions. The stations used in this study are shown in Fig. 1 along with principal geological/tectonic features identified in Table 1. In total there are 2073 stations used in this study. We measure Rayleigh wave group and phase speeds between all pairs of simultaneously operating stations based on ambient noise and also perform earthquake surface wave tomography beneath the NECESS array in Northeast China. The disparate components of this extensive data set require unified systematic data quality control (as discussed by Niu & Li 2011) and error estimation procedures, which we apply to all measurements including those from the earlier studies. We believe the procedures we have applied, including systematic data quality control and rigorous error analysis in the data presented in this paper, significantly improve the usefulness of the resulting model for other applications (e.g. wave simulations, predictions of other kinds of data and risk assessment).

Table 1. Tectonic zonation, blocks, and major basins in the region of study. Letters and numbers are found in Fig. 1(b).

Zones	Tectonic blocks	Major basins
Xiyu (Northwestern China)	Junggar Basin Block (A) Tianshan (B) Tarim Basin Block (C) Sayan Block (D) Altay Block (E) Alxa Block (F)	Junggar Basin (1) Tarim Basin (2) Turpan Basin (3)
Tibetan Plateau and Nearby Areas	Qilianshan Block (G) Qaidam Block (H) Songpan-Ganzi Terrane (I) Qiangtang Block (J) Lhasa Terrane (K) Chuandian Terrane (L)	Qaidam Basin (4) Qiangtang Tanggula Basin (5) Cuoqing Lunpola Basin (6) Qabdu Basin (7) Chuxiong Basin (8)
Southeastern Tibet	S. Yunnan Block (M) W. Yunnan Block (N)	Lanping-Simao Basin (9)
South China	Yangtze Craton (O) South China Block (P)	Sichuan Basin (10) Nanyang Basin (11) Jianghan Basin (12) East China Sea Basin (13) Pearl River Mouth Basin (14) Beibuwan Basin (15)
North China Craton and nearby seas	Ordos Block (Q) North China Plain (R) E. Shandong/Yellow Sea Block (S)	Jiuquan Minle Wuwei Basin (16) Ordos Basin (17) Bohaiwan Basin (18) Taikang Hefei Basin (19) Subei Yellow Sea Basin (20)
Northeastern China, Korean Peninsula, and the Sea of Japan	Yanshan Terrane (T) Xingan-East Mongolia Block (U) Northeast Asia (V) Ryuku Subduction Zone (W) Greater Xing'An Range (X) Lesser Xing'An Range (Y)	Songliao Basin (21) Temtsag Hailar Basin (22) Erlian Basin (23) Sea of Japan Backarc Basin (24) Tsushima Basin (25)

There is a long and rapidly growing list of studies of surface waves that have generated dispersion maps and derived 3D models in various regions across China. Some studies are based on ambient noise (e.g. Zheng *et al.* 2008, 2010b, 2011; Guo *et al.* 2009; Li *et al.* 2009; Huang *et al.* 2010; Yang *et al.* 2010, 2012; Guo *et al.* 2012; Luo *et al.* 2012; Karplus *et al.* 2013; Sun *et al.* 2013; Xie *et al.* 2013), others on earthquakes (e.g. Ritzwoller & Levshin 1998; Ritzwoller *et al.* 1998; Villasenor *et al.* 2001; Huang *et al.* 2003, 2009; Shapiro *et al.* 2004; Acton *et al.* 2010; Jiang *et al.* 2011; Li *et al.* 2013a,b; Legendre *et al.* 2014; Zhang *et al.* 2014), still others on both ambient noise and earthquakes (e.g. Yao *et al.* 2006, 2008, 2010; Zhou *et al.* 2012; Bao *et al.* 2013, 2015; Tang *et al.* 2013), and some are from joint inversions of surface waves and other types of data (e.g. Li *et al.* 2008; Obrebski *et al.* 2012; Wang *et al.* 2014; Deng *et al.* 2015; Guo *et al.* 2015). What is unique about the current study is that it is based on the largest set of surface wave information yet compiled across China and surroundings, it produces isotropic and azimuthally anisotropic dispersion maps with a uniform process of error estimation, and it generates a 3-D isotropic model that includes uncertainties in all variables. We believe that these characteristics and others qualify it as a reference model.

The structure of the paper is as follows. In Section 2, we discuss the extensive data set on which the model produced in this study is based. This includes its ambient noise and earthquake components and uncertainty estimates at all periods and locations across the study region. Sections 3 and 4 discuss the tomographic maps and the 3-D model. Finally, we discuss the content of the 3-D model in Section 5 and summarize the work in Section 6.

2 DATA, QUALITY CONTROL, TOMOGRAPHIC METHODS AND UNCERTAINTIES

2.1 Data processing

Ambient noise data processing is accomplished using the method described by Bensen *et al.* (2007) and Lin *et al.* (2008) with the primary caveat that pains are taken to minimize the impact of the Kyushu persistent microsiesmic source at Aso volcano in the centre of Kyushu (e.g. Zeng & Ni 2010, 2011; Kawakatsu *et al.* 2011), as described by Zheng *et al.* (2011). From the symmetric component of ambient noise vertical component cross-correlations, we measure Rayleigh wave group and phase speeds between 8 and 50 s period across the entire region of study. As described further below, however, the long period measurements, in particular, degrade in some regions, but in a way that is captured by the uncertainty measurements, and reduce in number.

Although ambient noise data and constraints exist across the entire study region, we have only compiled earthquake data in South China from Zhou *et al.* (2012) and parts of Northeast China beneath the NECESS array as described further below and in greater detail by Kang *et al.* (2016). The measurements from the NECESS array

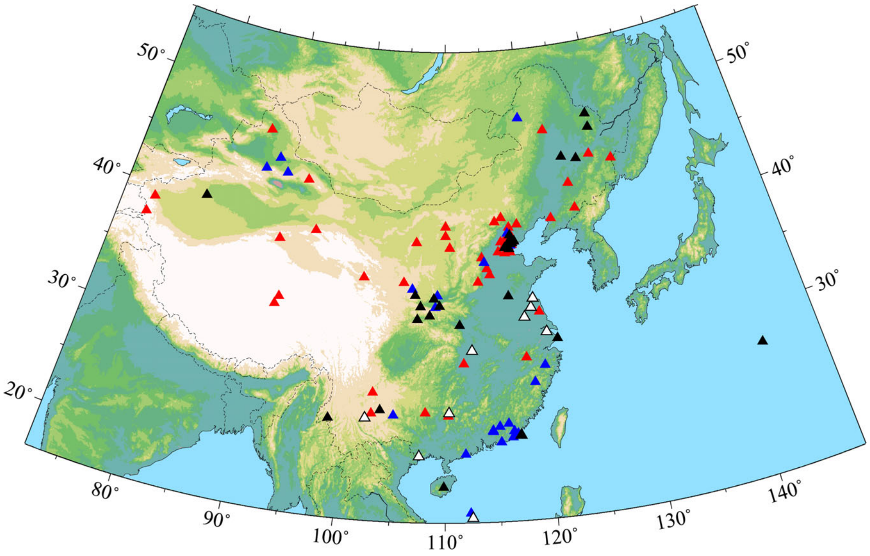

Figure 2. Locations of stations identified as problematic—red triangles: mislocation error; blue triangles: π phase error presumably a polarity error; white triangles: locations differ from different data sources; black triangles: unknown perhaps time variable problem with instrument responses.

are new to this study. Earthquake data are processed via eikonal tomography (Lin *et al.* 2009) in Northeast China or Helmholtz (Lin & Ritzwoller 2011b) tomography in South China, which differ based on whether a finite frequency correction is applied (e.g. Ritzwoller *et al.* 2011).

2.2 Core and augmented data set

We start the data compilation with Rayleigh wave phase and group traveltime measurements from the three earlier studies in eastern Asia: Yang *et al.* (2010) for Tibet; Zhou *et al.* (2012) for south China; and Zheng *et al.* (2011) for Northeastern China, Japan and the Sea of Japan. These data are referred to as our 'Core' measurements. In addition, we add to the Core measurements the 'Augmented' measurements, which derive from three sources. First, in preparing the studies of Yang *et al.* (2010, 2012) and Zheng *et al.* (2011), cross-correlations of ambient noise were computed across the entire CEArray (960 stations) using data from 2007 through 2009. These studies extracted and used only the measurements within Tibet and North/Northeast China, respectively. Therefore, as the first part of the Augmented data set we have the many paths between stations in separate regions (e.g. Tibet to North/Northeast China) and also paths that include South China that were not included in the Core data set. In addition, we have added measurements between stations in Tibet at periods not measured by Yang *et al.* (2010). Second, we have added measurements using 120 stations from the NECESS array and 30 stations from the Korean Seismic Network (KSN), computing cross-correlations of ambient noise both within each network and between them using data from September 2009 to August 2011. Third, we have combined 350 China Array stations in Yunan and Sichuan Provinces with 88 nearby CEArray stations to form a 438 station array and compute cross-correlation between these stations. We refer to these stations as 'China Array'. In summary, the Augmented data set increases the number of unique paths in the Core data set prior to quality control by a multiplier of 2–3.

2.3 Quality control of ambient noise data

One of the principal characteristics of the data set compiled in this study is that a single, uniform quality control procedure is applied to every dispersion measurement from ambient noise. This procedure consists of three key stages, which we call QC1, QC2 and QC3.

QC1 consists of two parts. First, we identify redundant paths, that is, measurements that exist between the same pairs of stations. This occurs in part because Zheng *et al.* (2011) and Zhou *et al.* (2012) make some measurements between the same pairs of stations but from different years. We resolve the ambiguity by choosing the measurement with the higher signal-to-noise ratio (SNR). The second part of QC1, which applies a procedure described by Zhou *et al.* (2012), is the identification of bad station information in which we measure the consistency between the Rayleigh wave phase traveltimes observed between nearby stations using ambient noise. We use this information to identify station location errors, polarity reversals and unknown factors that may be related to time varying instrument responses. Out of the 2073 stations in this study, about 5 per cent, or more accurately 107 stations, are identified as presenting erroneous information. Their locations and error types are presented in Fig. 2. Of these 107 stations, 57 stations are mislocated, 24 have a polarity error and 26 have unknown (perhaps time variable) phase errors. Additionally, there are 11 stations for which we have different locations (shifted by over 0.05°) from different data sources. In all cases, the stations are removed from our data set. In principle, some of these errors could be corrected, but in this data rich study we choose the more conservative option.

In QC2, we accept a group or phase speed measurement at a given period only if the SNR of the symmetric component of the cross-correlation at that period is greater than 15, where SNR is defined as in Bensen *et al.* (2007). This is a very conservative acceptance criterion. In addition, we accept a measurement at a given period only if the interstation spacing is greater than two wavelengths to ensure that the measurement is in the far-field and that the observed wave packet is sufficiently removed from zero correlation lag to obtain a meaningful dispersion measurement.

Finally, in QC3, we require our measurements to cohere with one another. We do this iteratively by constructing phase and group speed maps at each period, identifying and rejecting 1–2 per cent of the outliers in each of three iterations. Examples of distributions of misfits to measurements from the final estimated Rayleigh wave phase and group speed maps are presented in Fig. 3, illustrating that outliers have been rejected. The standard deviations of these

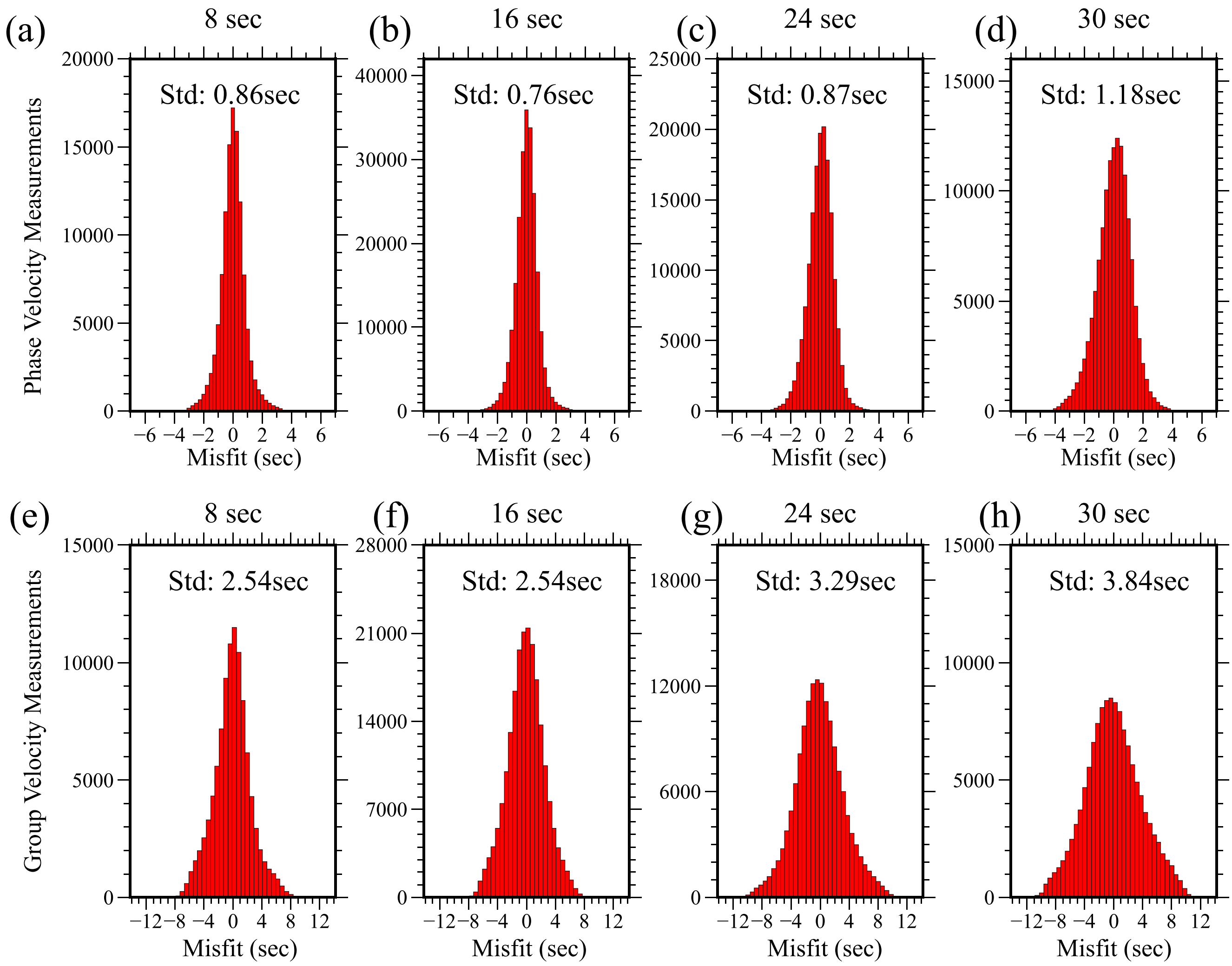

Figure 3. Examples of misfit histograms for the final data set: observed Rayleigh wave phase or group time minus predicted phase or group time (in s) computed using straight ray theory from the estimated phase or group speed map. The standard deviation of each misfit distribution is presented in each panel. Top row: phase speed measurements; bottom row: group speed measurements.

distributions are listed in Table 2. Phase traveltime misfits are less than 1 s, on average, at periods below 28 s and grow to about 1.5 s near 50 s period. Part of this increase is due to the reduction of SNR as periods increase, which increases random errors in phase speed measurements, but part is also due to the fact that average interstation distances grow with period.

Group traveltime misfits are considerably larger than for phase traveltimes because group times are a harder measurement to obtain reliably, as they depend on the amplitude of the wave packet envelope rather than the phase of the surface wave arrival. Group and phase traveltime misfits grow with period at approximately the same rate, but the standard deviation of group misfits is 2.5–3.5 times larger than phase misfits.

2.4 Earthquake data

We assimilate data from Zhou *et al.* (2012) who computed Rayleigh wave phase speed maps from 30 to 70 s period across South China using earthquake-based eikonal tomography (Lin *et al.* 2009.) In addition, we have also computed Rayleigh wave phase speed maps from 30 to 70 s period using data from the NECESS array, which are described further by Kang *et al.* (2016). These new measurements are based on Helmholtz tomography (Lin & Ritzwoller 2011b), which applies a finite frequency correction to the eikonal tomography method. Because long period data (>50 s period) only exist in South China and parts of Northeast China, the long period Rayleigh wave phase speed maps only exist in these two regions. In addition, we have no group speed measurements based on earthquake data so group speed curves terminate at or below 50 s period everywhere across the region of study.

The quality control procedure for earthquake data is described by Zhou *et al.* (2012) and Kang *et al.* (2016). We discard a Rayleigh wave measurement at a given period and for a given earthquake if its SNR is less than 8. Following Lin & Ritzwoller (2011b), the 2π phase ambiguity is resolved and phase measurements from particular earthquakes are discarded following criteria based on the curvature of the phase traveltime and amplitude surfaces across the array.

2.5 Tomographic methods

By ‘tomography’ we mean the transformation of phase and group speed (or time) measurements to phase or group speed maps at each period. The preferred tomographic method for ambient noise data is

Table 2. Number of unique paths and misfit as functions of period for ambient noise.

Period (s)	Final number of unique paths		Misfit (s)	
	Group	Phase	Group	Phase
8	99 929	114 499	2.54	0.856
10	152 555	172 225	2.53	0.845
12	185 235	204 790	2.55	0.775
14	204 102	221 233	2.47	0.751
16	212 290	227 940	2.54	0.757
18	219 614	227 007	3.11	0.809
20	212 329	218 990	3.22	0.819
22	174 309	177 860	3.20	0.800
24	154 435	157 861	3.29	0.871
26	138 559	141 719	3.40	0.947
28	125 423	128 770	3.59	1.029
30	129 618	134 885	3.84	1.180
32	92 793	96 666	3.81	1.182
35	96 337	102 213	4.11	1.340
40	64 766	70 182	4.38	1.455
45	43 247	47 379	4.59	1.556
50	22 574	25 504	4.73	1.662

eikonal tomography (Lin *et al.* 2009) because it yields local uncertainty estimates both for isotropic and azimuthally anisotropic phase speeds. Eikonal tomography is based on geometrical ray theory, which models rays bent by lateral variations in structure and produces meaningful uncertainty estimates in the resulting dispersion maps. However, eikonal tomography works only for phase speeds and requires regular station spacing for optimal performance. Because we seek group velocity maps in addition to phase velocity maps and station spacing is irregular across much of the study region, we apply the traditional ray theoretic method of Barmin *et al.* (2001) to all ambient noise data in this study and results are presented on a 0.5° × 0.5° grid. This method produces isotropic phase and group speed maps with resolution estimates as well as azimuthal anisotropy maps, but does not estimate data uncertainties and models rays only along great-circle paths.

Station spacing across parts of East China is sufficiently regular to apply eikonal tomography to estimate phase speed maps, an example of which for the 20 s Rayleigh wave is presented in Fig. 4(a). Previous studies have shown that finite frequency corrections (produced, for example, by the Helmholtz tomography method) are not required below 40–50 s period for on-continent ambient noise derived measurements (e.g. Lin & Ritzwoller 2011b) and they will not be applied here. The 20 s Rayleigh wave phase speed map using the traditional ray theoretic method of Barmin *et al.* (2001) is presented in Fig. 4(b) for comparison with Fig. 4(a). The choices of damping and regularization in Barmin's method are guided to optimize agreement between the maps. The maps are generally quite similar, with differences scattered throughout the maps at small length scales (Fig. 4c). The mean difference between the maps is 4 m s^{-1} or 0.1 per cent and the standard deviation of the difference is 17.5 m s^{-1} or 0.5 per cent, as the histogram in Fig. 4(d) illustrates. As reported in Section 2.6, these differences lie within data uncertainties, when the uncertainties are properly defined. The difference of the mean may be due to the effect of off great-circle propagation, but it is below what we consider to be a significant bias. On this basis, we apply the traditional ray theoretic method of Barmin *et al.* to produce all ambient noise maps presented here but take pains to estimate uncertainties in the maps, as discussed in Section 2.6. Tomographic maps for both isotropic and azimuthally anisotropic wave speeds are presented in Section 3.

A similar comparison of estimates of azimuthal anisotropy for Rayleigh wave phase speed at 20 s period between eikonal tomography and the method of Barmin *et al.* (2001) is presented in Fig. 5 in a region where eikonal tomography performs well. The average of the absolute value of the difference in the observed fast axis directions of azimuthal anisotropy between the two methods is 11.8° and the average of the difference in the amplitudes between the methods is about 0.3 per cent. Lin & Ritzwoller (2011a) present results from random simulations of noisy realizations of azimuthal anisotropy and argue that differences at this level are expected given the size of uncertainties in estimates of the amplitude and fast axis direction of azimuthal anisotropy. Therefore, we conclude that the traditional tomographic method of Barmin *et al.* presents sufficiently accurate and precise results to act as the basis for the model presented here.

Using Helmholtz tomography we produce new Rayleigh wave phase speed maps from 30 s to 70 s period based on earthquake data beneath the NECESS array in Northeast China, also on a 0.5° × 0.5° grid. We also assimilate the previous earthquake-derived phase speed maps produced by Zhou *et al.* (2012) in South China based on eikonal tomography from 30 s to 70 s period. Therefore, spatial coverage at periods greater than 50 s is patchy across East China, as the tomographic maps presented in Section 3 illustrate. An example of an earthquake-derived Rayleigh wave phase speed map at 40 s period is shown in Fig. 6(a) and compared with the ambient noise derived map in Fig. 6(b). The earthquake-derived map only exists beneath the NECESS array whose outline is drawn in Figs 6(a) and (b). Differences between the maps are shown in map and histogram forms in Figs 6(c) and (d), respectively. As discussed in Section 2.6, these differences lie within those expected given data uncertainties, which we interpret to indicate agreement between the earthquake and ambient noise based tomography methods.

2.6 Uncertainty estimates for dispersion curves

Data uncertainties include both random and systematic errors. In this study, we measure the uncertainties in the local phase and group velocities, which compose the direct input for the inversion of 3-D model, using eikonal and Helmholtz tomography methods. In these methods, surface wave traveltimes are converted into local phase velocities by applying a set of operators applied to the traveltime and amplitude fields (e.g. gradient). In the conversion, random errors in traveltimes generate scatter in the local phase velocity measurements. Thus, by analysing the scattering of the local phase velocity measurements we estimate uncertainties in the phase velocities directly without the need to measure the errors in the traveltimes. Because only random errors are thus considered in the estimation process, we scale up the uncertainties so measured as suggested by Lin *et al.* (2009).

For earthquake data, we obtain phase velocity uncertainties estimated from the eikonal and Helmholtz tomography methods directly in Northeast China and South China, respectively. For ambient noise, the situation is unfortunately more complicated; we do not have uncertainty estimates everywhere because eikonal tomography only performs well across a subset of the study region. Therefore, we start with the uncertainties estimated from eikonal tomography wherever it can be applied and, following Lin *et al.* (2009), scale up the raw uncertainties by a factor of 2 to account for the facts that individual measurements of phase traveltimes at particular locations are not independent and only random errors are initially considered

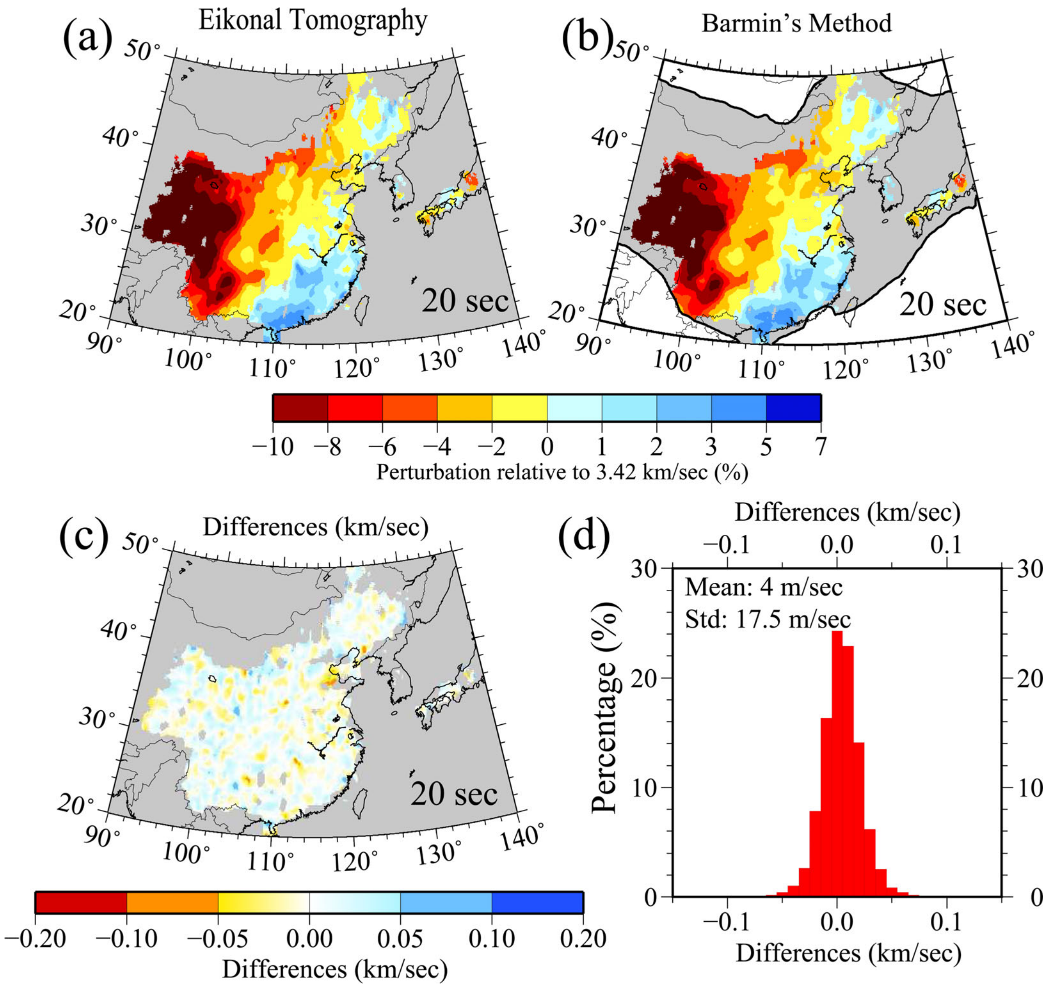

Figure 4. Comparison between the 20 s Rayleigh wave isotropic phase speed maps constructed from ambient noise measurements using (a) eikonal tomography and (b) the traditional ray theoretic tomography method of Barmin *et al.* (2001) in the region where eikonal tomography performs well, presented as percent deviations from 3.42 km s^{-1}. (c) The difference between these two maps: Barmin's method minus eikonal. (d) Histogram of the differences between the maps, with the mean and standard deviation indicated.

in the uncertainty estimates. Because eikonal tomography cannot be applied everywhere across the study region, we extrapolate the uncertainty estimates where we have them to locations where we do not. To do this, we are guided by local estimates of resolution, $R(r)$, which we do have everywhere using the method of Barmin *et al.*

We find that uncertainties estimated with eikonal tomography are approximately constant as a function of location wherever data coverage is high. In an unpublished result based on USArray data we find that uncertainties scale approximately with local path density or resolution. Therefore, where eikonal tomography cannot be applied we scale up the uncertainties based on local data coverage. Fig. 7(a) shows that path density across the study area is quite variable, with the best coverage occurring where we are able to apply eikonal tomography. Eikonal tomography does not provide an estimate of resolution, but the method of Barmin *et al.* (2001) generates a resolution map for each target location to which a 2-D Gaussian is fit. The resolution map is determined from the resolution matrix for each grid location r. Twice the standard deviation of the fit Gaussian is interpreted as the local resolution, $R(r)$, at position r. Local resolution defined in this way is a complicated function of path density, local station spacing and the chosen grid spacing. However, in the data rich regions of this study, local resolution is approximately the grid spacing, which averages ~50 km. An example at 20 s period is shown in Fig. 7(b), where the best resolution is about 50 km, which is found across much of East China. We refer to this best resolution (which is equal to the grid spacing) across a tomographic map (~50 km) as the optimal resolution at a given period, R_{optimal}.

To estimate local uncertainties we apply the following two step procedure separately at each period (τ). (1) In regions of optimal resolution where local resolution $R(r)$ is equal to the grid spacing (R_{optimal}), we compute the spatial average of the uncertainties from eikonal tomography across that region and assign that value everywhere across that region. This procedure yields a set of period dependent uncertainties $\sigma_{\text{optimal}}(\tau)$ for all points in the region with optimal resolution. (2) Outside the region with optimal resolution, eikonal tomography typically does not perform well. For these areas, we extrapolate the uncertainty information from the region with optimal resolution. To do this we apply an empirical relationship that scales resolution to uncertainty using the following formula:

$$\sigma(r) = \left(\frac{R(r)}{R_{\text{optimal}}}\right)^{k} \sigma_{\text{optimal}}. \tag{1}$$

Here, $\sigma(r)$ is the position dependent uncertainty that we seek outside the region of optimal resolution, σ_{optimal} is the uncertainty in the regions with optimal resolution, $R(r)$ is position dependent resolution determined using the method of Barmin *et al.*, R_{optimal}

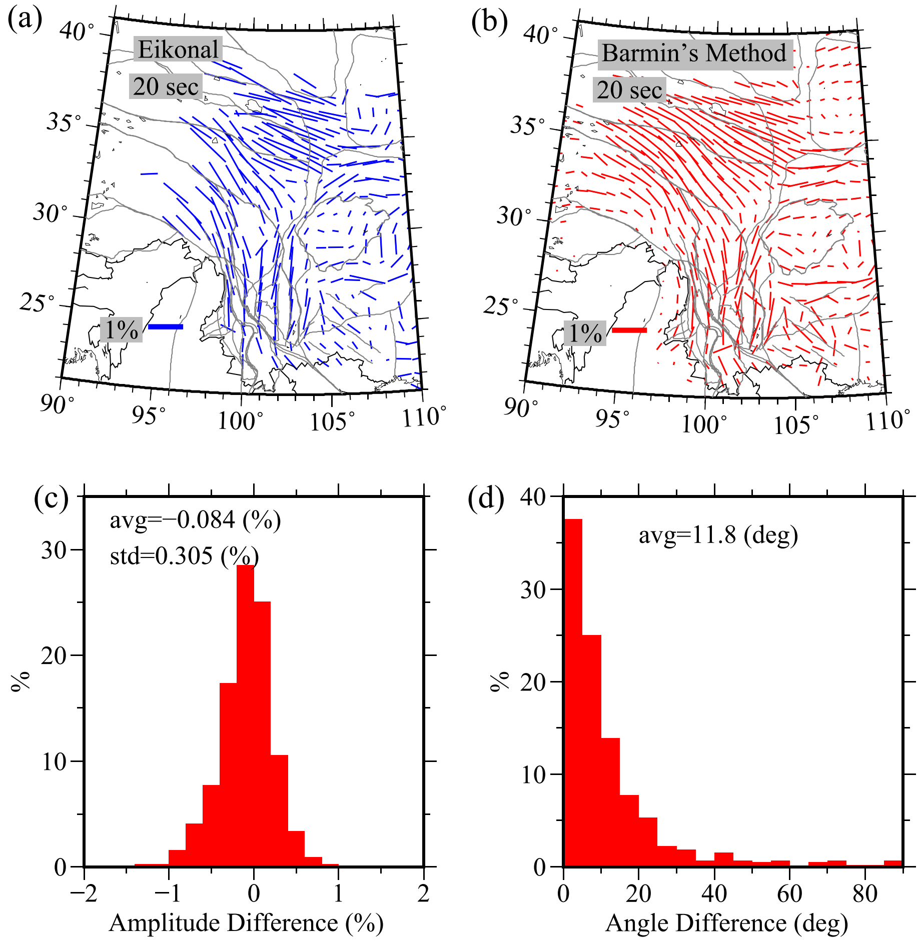

Figure 5. (a,b) Like Fig. 4, but this is a comparison between eikonal tomography and the method of Barmin *et al.* (2001) for azimuthal anisotropy, which is plotted so that the length of each bar is proportional to the amplitude of azimuthal anisotropy (see inset in each panel showing the length scale) and the direction of each bar points in the fast-axis directions. (c,d) Histograms of the differences in the amplitude and fast-axis direction between the two tomographic methods: Barmin's method minus eikonal.

is the optimal resolution across the study region what is equal to the grid spacing and k is an unknown positive factor that scales the local uncertainties though local resolution.

We used USArray to test the efficacy of eq. (1) to scale resolution to uncertainty and to find the power k. We applied both eikonal tomography (to estimate phase velocity uncertainty) and the method of Barmin *et al.* (to estimate resolution) and systematically removed stations from USArray re-running both types of tomography after each decrement in station density. We found that eq. (1) represents the relationship between resolution and phase velocity uncertainty well, on average, with $k = 1$.

As discussed later, we truncate the dispersion maps where local resolution is worse than 160 km, which is about three times the optimal resolution. Thus, for example, the 20 s phase speed map is reduced spatially relative to the resolution map seen in Fig. 7(b). With a local resolution of 160 km, therefore, uncertainties will be scaled up by about a factor of 3 relative to uncertainties where resolution is optimal. Thus, no part of the region of study will have an uncertainty more than about 3 times higher than the uncertainty in the region with optimal resolution.

Example maps of phase speed uncertainties computed in this way are shown at periods of 10 s and 30 s in Figs 8(a) and (b), where at these periods the uncertainties are based on ambient noise data alone. Note that uncertainties are constant across large regions of these maps, which are near optimal resolution, and then increase towards the periphery of the maps. At 40 s period (Fig. 8c) the uncertainties are based on ambient noise results where earthquake derived results do not exist, but are the average of uncertainties from ambient noise and earthquakes data where both types of measurements exist. Uncertainties using earthquake data are slightly lower than using ambient noise data, at least in South China and Northeast China where the earthquake data exist. In the peripheral parts of the maps uncertainties from ambient noise data increase strongly. Note that in this intermediate period range between 30 and 50 s period, where we have uncertainty estimates from both types of data, we apply the same linear weighting scheme to compute a weighted average uncertainty that we apply to the phase speeds, described in Section 2.7. At 60 s period uncertainties are from earthquake data alone. The uncertainty map in Fig. 8(d), therefore, demarcates the locations of earthquake results. The area of higher uncertainty (dark blues) in the middle of South China results from a station gap at that location after the removal of erroneous stations, as can be seen in Figs 1(a) and 2.

Uncertainties estimated for group speed maps from ambient noise are scaled from the local uncertainties $\sigma(r)$ in phase speed. The scaling factor is 2.5 because misfits to group velocities tend to be 2.5–3.5 times larger than for phase velocities across most regions we have studied (Fig. 3 here, and similar results in earlier studies;

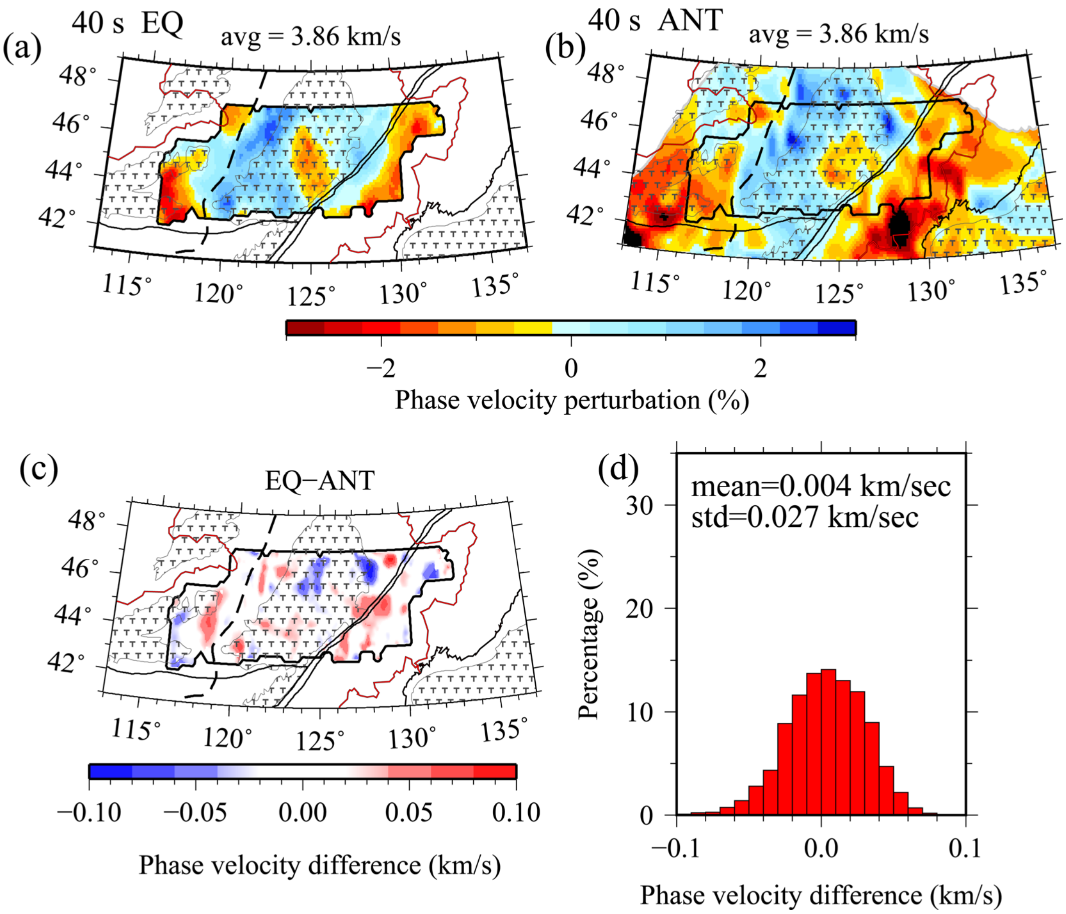

Figure 6. Comparison between the 40 s Rayleigh wave isotropic phase speed maps constructed from (a) earthquake based measurements interpreted through Helmholtz tomography and (b) ambient noise measurements interpreted through the topographic method of Barmin *et al.* (2001). The earthquake results are based on NECESS data and the location of the array is outlined in (a) and (b). (c) Difference between the results of these two data sets and tomographic methods: earthquake minus ambient noise results. (d) Histogram of the differences in (c), with statistics presented.

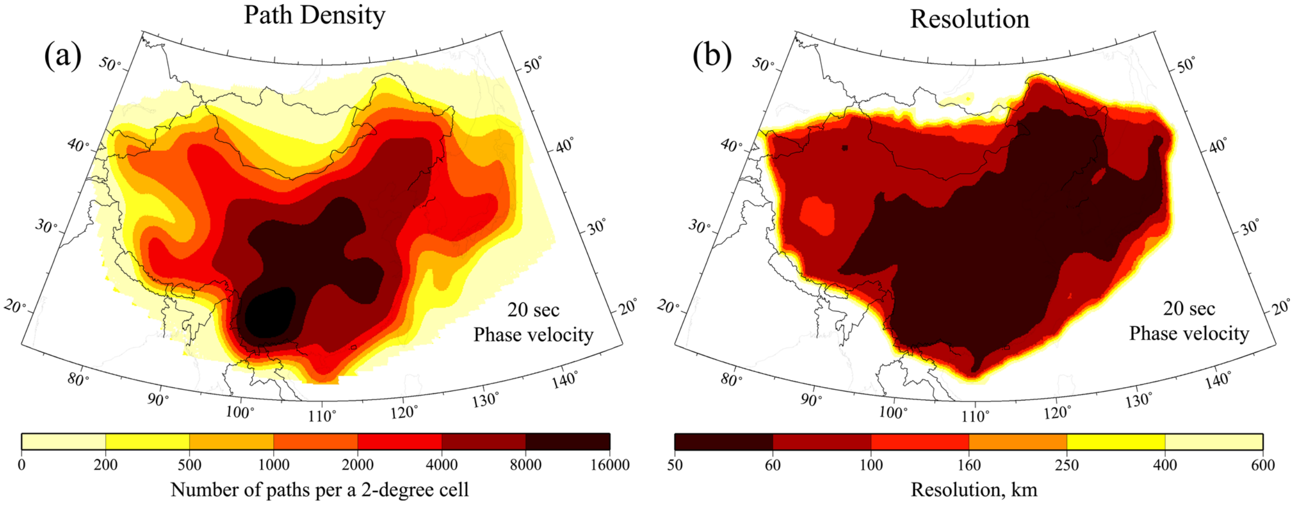

Figure 7. Examples of path density and resolution maps. (a) Path density estimated for the 20 s Rayleigh wave phase speed map in units of the number of paths contained in each 2° square cell (~50 000 km^2). (b) Estimated resolution for the 20 s Rayleigh wave phase speed map, where resolution is defined as twice the standard deviation of the 2-D Gaussian fit to the resolution surface at each grid node.

e.g. Moschetti *et al.* 2010). The procedure is a little more subtle than this because phase and group resolutions differ somewhat and we use the group resolution to guide this process. Examples are shown in Figs 9(a) and (b).

Uncertainties averaged across the study region are summarized in Fig. 9(c). Group speed uncertainties are for ambient noise results alone and minimize near 20 s period, but increase sharply at periods above about 30 s. Phase speed uncertainties also minimize around

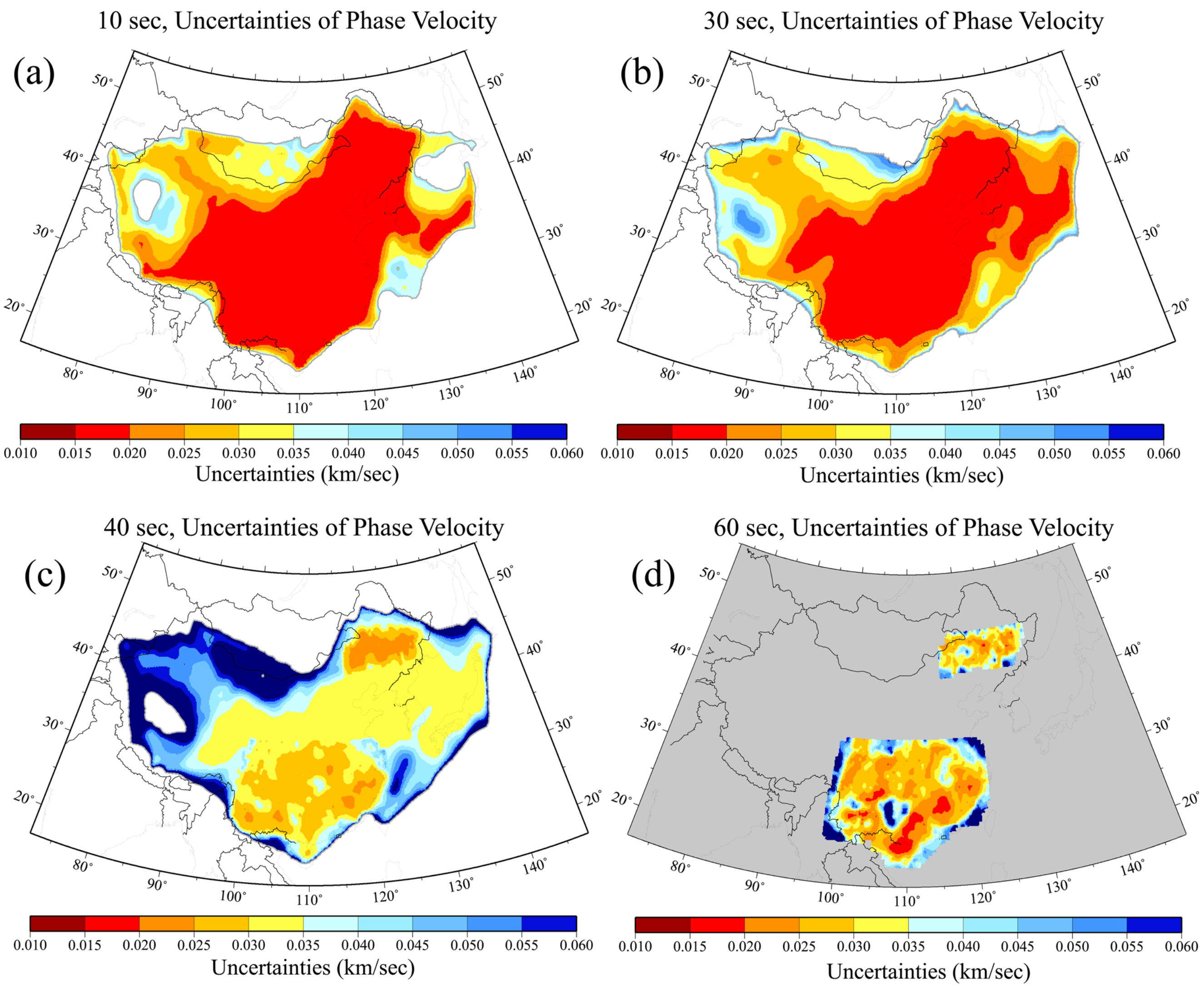

Figure 8. Estimated one standard deviation uncertainties of Rayleigh wave phase speed at periods of (a) 10 s, (2) 30 s, (3) 40 s and (4) 60 s. At 60 s period, measurements are from earthquakes alone and the map identifies the area where earthquake measurements exist. At 10 and 30 s period, uncertainties derive from ambient noise data alone and at 40 s period uncertainties equally weight contributions from ambient noise and earthquake data.

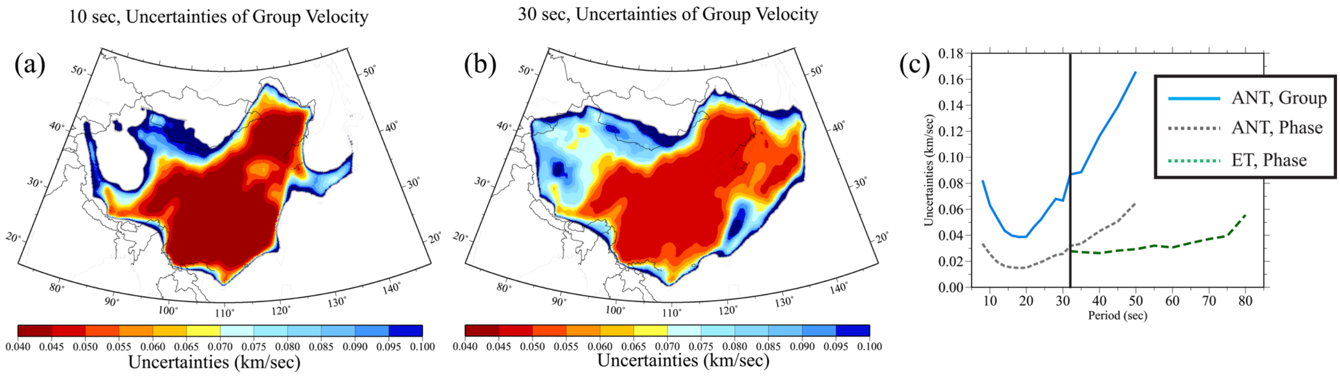

Figure 9. (a,b) Similar to Fig. 8, but uncertainties here are for Rayleigh wave group speeds at 10 and 30 s period, from ambient noise tomography (ANT) alone. (c) Rayleigh wave group and phase speed uncertainties averaged across the study region are presented as a function of period. Above 30 s period, phase speed uncertainties are for ambient noise and earthquake (ET) tomography are presented separately, where ambient noise uncertainties are averaged across the entire region of study and earthquake uncertainties are averaged only where such measurements exist (*cf.* Fig. 8d).

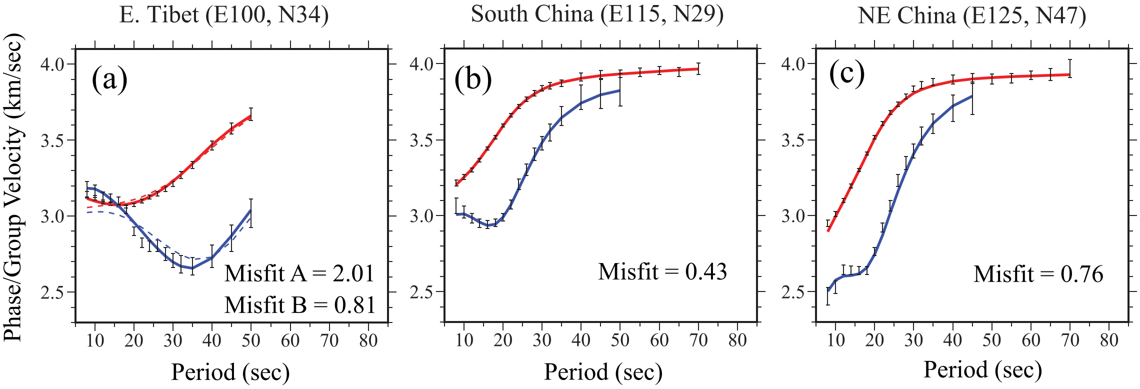

Figure 10. Examples of Rayleigh wave group and phase speed measurements presented as one standard deviation error bars for the three locations (a, Tibet; b, South China; c, Northeast China) identified by stars in Fig. 1. Solid curves are computed from the mean of each posterior distribution at each location (red lines, phase speed; blue lines, group speeds), which is shown in Fig. 17. For the location in Tibet, two curves are plotted: dashed line, Model A—crustal monotonicity constraint; solid line, Model B—no monotonicity constraint. Misfits, defined by eq. (2), are labelled in each panel. The larger Misfit on the Tibet panel is for the model with the crustal monotonicity constraint and the other is for the model without this constraint.

20 s period and increase with period, but not as strongly as for group speeds. Phase speed uncertainties based on earthquake data are flatter still with period and, on average, lower than uncertainties based on ambient noise data in the period band of overlap. However, this is because ambient noise results extend into regions with poor data coverage where uncertainties are higher and the average uncertainty reflects these regions. Uncertainties based on ambient noise in regions where there are earthquake data are slightly higher than earthquake based uncertainties.

The Rayleigh wave phase speed uncertainties we estimated (e.g. Fig. 8) capture differences in the phase speed maps that result from the application of different tomographic methods to ambient noise data or from different data sets (ambient noise versus earthquake data). For example, at 20 s period the average Rayleigh wave phase speed uncertainty is $\sim$14 m s^{-1} (Fig. 9c) and the standard deviation of the difference between the maps derived from eikonal and traditional tomography is about 18 m s^{-1}, as seen in Fig. 4(d). Assuming that the maps from eikonal and traditional ambient noise tomography have independent Gaussian error processes with a standard deviation of 14 m s^{-1}, the standard deviation of their difference is expected to be about $\sqrt{2} \times 14$m s^{-1} $\sim$ 20 m s^{-1}. Thus, with a standard deviation of their difference of 18 m s^{-1}, the 20 s period maps differ approximately as expected given the estimated uncertainties. Similarly, at 40 s period beneath the NECESS array the average Rayleigh wave phase speed uncertainty is $\sim$22 m s^{-1} (Fig. 8c) for both ambient noise and earthquake derived results; thus the maps are expected to differ with a standard deviation of about $\sqrt{2}$ larger than this value, or about 31 m s^{-1}. The standard deviation of the difference between the maps derived using ambient noise and earthquake data is 27 m s^{-1}, as seen in Fig. 6(d), which again agrees with our uncertainty estimates.

Holes in the phase and group speed uncertainty maps (e.g. Figs 8 and 9) and in the phase and group speed maps appear where the maps are truncated due to resolution degrading to values greater than 160 km.

One standard deviation uncertainty estimates are presented as error bars in the Rayleigh wave phase and group speed curves presented for three locations in Fig. 10. Error bars for group speeds are seen to be larger than for phase speeds and they are larger at longer periods. We show in Section 4 that on average the data are fit at about the 0.8σ level, which we argue provides evidence that the error bars realistically capture uncertainty in the measurements.

2.7 Resulting local dispersion curves

Examples of final group and phase speed maps for both isotropic and azimuthally anisotropic Rayleigh waves are discussed in Section 3. The data used in the inversion for the 3-D model are local Rayleigh wave phase and group speed curves with uncertainties; examples from three locations across China are presented in Fig. 10, which illustrate the geographical variability of the curves. The dispersion curves across Tibet (e.g. Fig. 10a) are distinguished by the effect of the anomalously thick crust so that the Airy phase (group velocity minimum) appears at much longer periods than elsewhere across the study region. The Northeast China curves in Fig. 10(c) come from the Songliao sedimentary basin. The sediments in the basin reduce phase and group speeds at short periods at this location. The structure beneath South China is simpler, which is reflected in simple dispersion curves (e.g. Fig. 10b).

At 30 s period and below local Rayleigh wave speeds and uncertainties derive entirely from ambient noise data everywhere and at 50 s and above they derive entirely from earthquake data where such information exists. For intermediate periods ($30 < \tau < 50$), wave speeds and uncertainties are averaged from both data sets. Across most of the region of study, earthquake results do not exist, but where they do exist we compute a weighted average of both velocity estimates and uncertainties where the weights applied to ambient noise and earthquake derived values change linearly with period. For example, at 30 s period the ambient noise weight is 1 and the earthquake weight is 0, at 40 s period both the ambient noise and earthquake weights are 0.5, and at 50 s period the ambient noise weight is 0 and the earthquake weight is 1. The fact that ambient noise and earthquake contributions to the resulting dispersion curves vary spatially and with period is an unfortunate complication in this study, but reflects the large spatial extent of this study, the long time frame of the observations, and the highly variable nature of the instrumentation and the data sources.

3 TOMOGRAPHIC MAPS

Examples of Rayleigh wave phase speed maps at a variety of periods are presented in Fig. 11. Ambient noise derived results exist everywhere across the maps at periods of 50 s and below and earthquake based results exist between 30 s and 70 s period only in parts of South and Northeast China. Therefore, the maps shown in Fig. 11

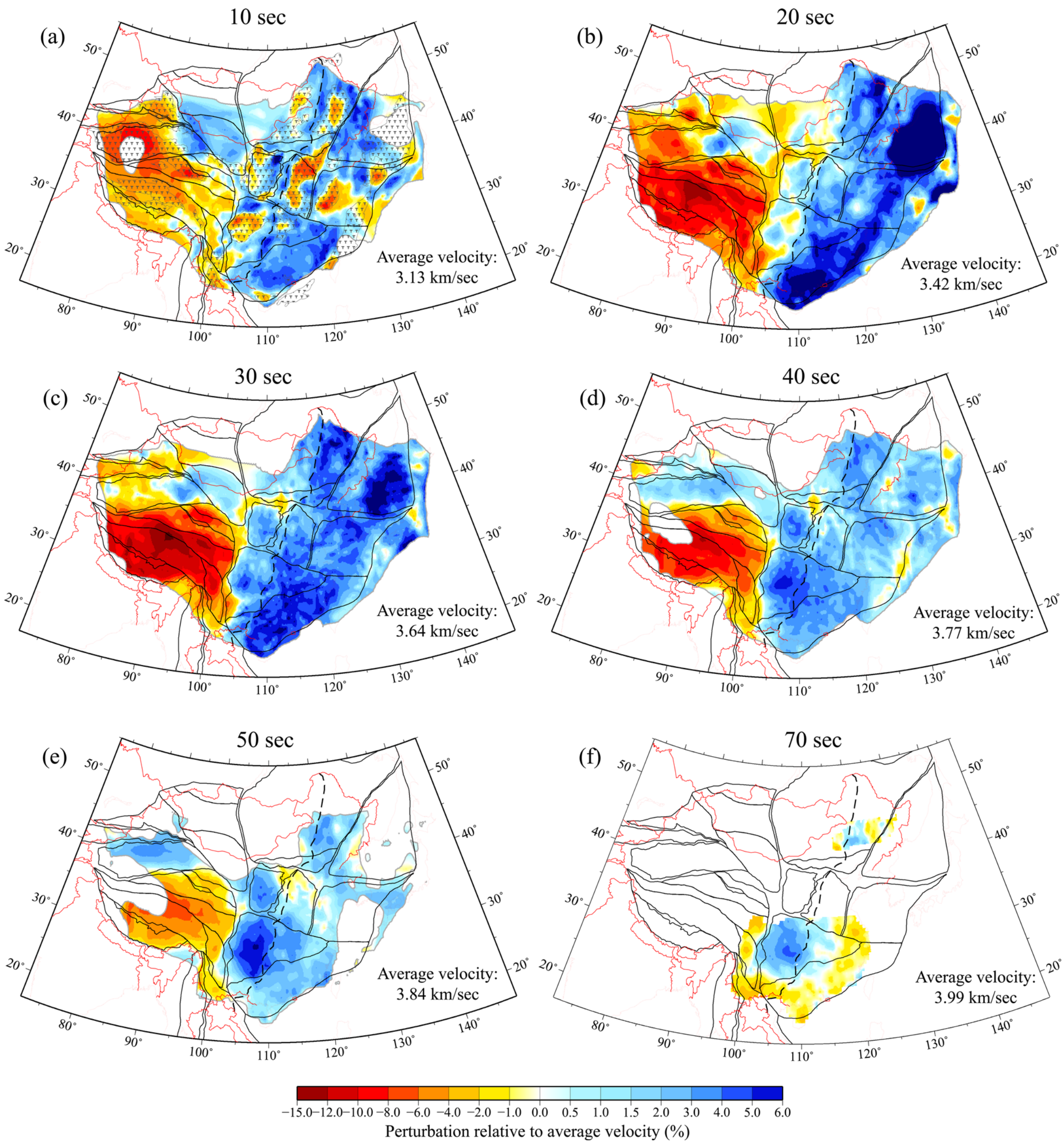

Figure 11. Estimated Rayleigh wave phase speed maps at a selection of periods presented as percent perturbations relative to the mean labelled on each map. At 30 s period and below, maps derive from ambient noise data alone, at 70 s period the map derives from earthquake data alone, at 50 s period the map derives from earthquake data where they exist and ambient noise elsewhere, and at 40 s period the map derives from both ambient noise and earthquake data weighted equally where both data sets exist. The overplotted tectonic features and basins are identified in Fig. 1(b) and Table 1.

at 30 s and below derive exclusively from ambient noise data, the map at 40 s derives from both ambient noise and earthquake data weighted equally where both types of data exist and from ambient noise elsewhere, the map at 50 s derives from earthquake data where it exists and ambient noise elsewhere, and the map at 70 s period derives from earthquake data alone. Maps are presented at each period wherever local resolution is estimated to be better than 160 km. At 10 s period (Fig. 11a), Rayleigh wave phase speed is highly sensitive to the existence and character (thickness, lithology) of sedimentary basins with the Junggar, Tarim, Sichuan, Jianghan, North China (Bohaiwan, Taikang Hefei), and Songliao basins appearing prominently onshore along with basins offshore (East China Sea, Subei Yellow Sea, Tsushima). Phase speeds from 20 to 40 s period (Figs 11b–d) reflect crustal shear wave speeds and notably crustal thickness, where lower phase speeds indicate thicker crust. At 50 s and higher (Figs 11e and f), the maps are increasingly sensitive to upper mantle shear wave speeds. At periods of 20 s and higher, phase speed maps are dominated by an East-West dichotomy across the study region, which reflects the much thicker crust beneath Tibet. Smaller scale anomalies with smaller amplitudes are apparent within the eastern and western parts of the study region, characteristic of variations between and within tectonic units. For example, at 50 s period the highest Rayleigh wave speeds appear in the western Yangtze craton beneath the Sichuan basin, presumably representing the core of the craton. A separate high-velocity anomaly exists at 50 s period beneath the Ordos block. The 70 s period phase speed map is derived exclusively from earthquake data and is confined to parts of South and Northeast China.

The Rayleigh wave group speed maps presented in Fig. 12 derive exclusively from ambient noise data. They are similar to the phase

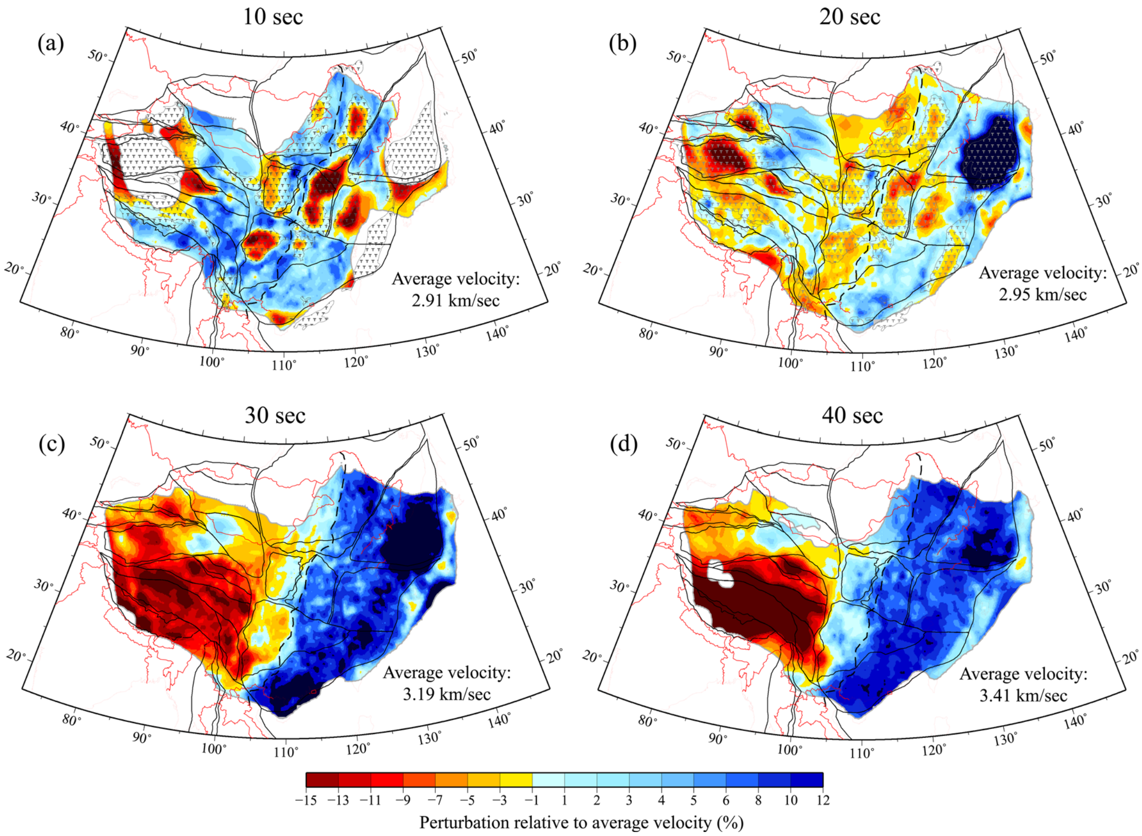

Figure 12. Similar to Fig. 11, but Rayleigh wave group speed maps are presented at the indicated periods and all maps are derived from ambient noise.

speed maps except group speed at a given period is sensitive to shallower structure than phase speed at the same period. Thus, the 20 s group speed map presented in Fig. 12(b) retains significant sensitivity to sedimentary structure unlike the 20 s phase speed map and is less dominated by the East-West dichotomy. The 10 s group speed map (Fig. 12a) displays sedimentary basins even more clearly than the 10 s phase speed map (Fig. 11a). The shallower sensitivity of group speed measurements makes them particularly useful to constrain sedimentary structure. The East-West dichotomy across the study region asserts itself strongly on group speed maps at periods of 30 s and above (e.g. Figs 12c and d).

A significant technical aspect in the construction of the isotropic group and phase speed maps is the simultaneous estimation of azimuthal anisotropy. In some areas where azimuthal coverage is not optimal, particularly in parts of Tibet, whether azimuthal anisotropy is estimated simultaneously with the isotropic maps strongly affects the characteristics of the isotropic maps. Here, where our focus is the development of an isotropic reference model, we estimate azimuthal anisotropy to ensure that the isotropic maps and resulting model are not biased by anisotropy. However, the maps of azimuthal anisotropy are interesting intrinsically and are produced for potential later use. Figs 13a–c summarizes the observations of Rayleigh wave azimuthal anisotropy at periods of 10, 20 and 30 s within the contour of 1000 paths per 2° × 2° cell. Outside the contour, azimuthal anisotropy is not well determined due to low path density, which we take as proxy for poor azimuthal coverage. As a result, the isotropic velocity measurements outside the contour will be more likely to be biased by the azimuthal anisotropy.

The maps shown in Fig. 13 are sensitive to the crust and uppermost mantle for most of the study area except Tibet, where the principal sensitivity is to the crust. The anisotropy at 10 s period is mainly sensitive to the uppermost crust, and its lateral variation is well correlated with the major geological provinces; for example, anisotropy is strongest in the Tibetan Plateau and weakens in eastern China. Relatively strong anisotropy is observed beneath the Bohaiwan and Songliao basins and along the boundary between the Yangtze Craton and the South China Fold Belt. At longer periods (e.g. 30 s), anisotropy is weaker than at shorter periods, although it remains strong in the Tibetan Plateau and increases in Japan. Unlike the amplitude of azimuthal anisotropy, the direction of anisotropy is generally consistent between the three periods. This includes NW–SE fast directions across northern Tibet, nearly N–S directions in southeastern Tibet, and NW–SE directions in Japan, which are subparallel to the Japan-Ryukyu subduction direction. The purpose of this paper is to produce an isotropic reference model, and further discussion on anisotropic structure is beyond its scope.

4 3-D MODEL

What emerges from surface wave tomography is a set of Rayleigh wave group and phase speed curves with uncertainties, such as the examples shown in Fig. 10. For most of the region of study these curves extend from 8 to 50 s period, but in parts of South China and Northeast China they extend up to 70 s period. In addition, in some places measurements do not extend down to 8 s period. Considerable care has been taken with data quality control and estimating realistic uncertainties. At their best, where eikonal tomography works, the estimated uncertainties reflect the repeatability of the measurements and allow a frequentist interpretation. Elsewhere, however, uncertainties are extrapolations from regions where eikonal tomography delivers uncertainty information. In these regions they represent our degree of belief in the measurements.

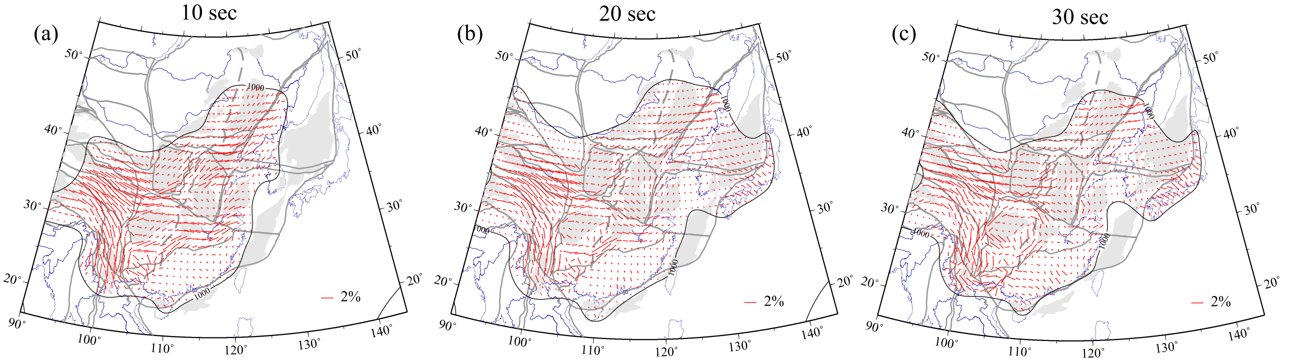

Figure 13. Estimates of azimuthal anisotropy for Rayleigh wave phase speeds at 10, 20 and 30 s period, determined using ambient noise data. The regions where azimuthal anisotropy estimates are considered reliable are outlined with the black lines where path density is greater than 1000 paths per 2° square cell (*cf.* Fig. 7a).

The 3-D model we present here is produced via a Bayesian Monte Carlo inversion so that a distribution of models is generated that fit the data acceptably. Within this framework, seismic models are conceived as random variables about which only probabilistic statements are made. As described in greater detail by Shen *et al.* (2013a,b), the inversion progresses in three steps that we briefly summarize here. (1) The starting point is the generation of the prior distribution of candidate models which at each point on a 0.5° × 0.5° grid represents the range of models we wish to consider. The prior distribution is governed by constraints on the range of values that model variables can take and relations between the variables. In this paper we choose the allowed range of model variables to be quite broad so that the posterior distribution, notably model uncertainties, will represent the information found in the likelihood function, that is, the data, much more strongly than prior constraints. We believe that this is consistent with our intent to produce a reference model, which is designed for use by other researchers. (2) A chain of candidate models in the prior distribution is selected by a random walk in model space guided by the Metropolis algorithm (Mosegaard & Tarantola 1995), which is the 'Monte Carlo' aspect of this inversion. For each model selected, theoretical Rayleigh wave group and phase speed curves are computed using the forward modelling code of Herrmann (Herrmann 2013) and the χ^2 misfit to the observed curves is determined. An individual chain of models terminates when an equilibrium in model misfit is attained and we then tabulate the models near equilibrium. A new chain is then begun at a random model from the prior distribution and the process repeats. (3) The posterior distribution is determined by further considering the tabulated models compiled in Step 2. The best fitting model is identified at each grid node and models there are accepted if their misfit is less than 50 per cent higher than that of the best fitting model. The posterior distribution is then summarized in terms of the mean and standard deviation of each model variable or combination of model variables (e.g. Vs at different depths, sedimentary thickness, crustal thickness, etc.). In addition, correlations between model variables and their combinations can be computed.

In this section, we present examples of aspects of this process and show the mean and standard deviation of some of the principal model variables across the region of study.

4.1 Model parametrization

The starting model around which we perturb is compiled from a combination of three earlier models of Tibet (Yang *et al.* 2012), South China (Zhou *et al.* 2012) and North/Northeast China extending to Japan (Zheng *et al.* 2011). The models in South and North/Northeast China are on the same 0.5° × 0.5° grid we use, but we interpolate the model of Tibet from 1° × 1° onto our grid.

The model is primarily in Vs with Vp and density scaled to it, as discussed shortly. Because only Rayleigh wave data are used in the inversion, formally speaking the shear velocities are Vsv rather than Vs, but we refer to them as Vs throughout. In other words, radial anisotropy is assumed to be zero, therefore Vp = Vpv = Vph, Vs = Vsv = Vsh and $\eta = 1$. Sedimentary basins are represented with three unknowns: thickness and the top and bottom Vs values that change linearly with depth in the basin. Shear wave speeds in the crystalline crust are represented with five cubic B-splines on the continent and four B-splines offshore. The thickness of the crystalline crust is also a free variable in the inversion. Mantle shear wave speeds from right below the Moho to 200 km depth are described by five cubic B-splines. Below 200 km, the model is a half-space where shear waves speed is constant and equal to the value at 200 km depth. Vp is computed from Vs such that Vp/Vs = 2.0 in the sediments, Vp/Vs = 1.79 in the mantle influenced by AK135 (Kennett *et al.* 1995), and in the crystalline crust the relationship between Vp and Vs is taken from Brocher (2005). Density (ρ) is also computed from Vs using the relations provided by Brocher (2005) in the sediments and crystalline crust. In the mantle, density is determined based on the partial derivative of ρ with respect to Vs extracted from Hacker & Abers (2004) and applied relative to AK135. With these rules, we determine a Vp and ρ model for every Vs model, and therefore for a distribution of Vs models we also have a distribution of models of Vp and ρ. However, because Vp and ρ are deterministically related to Vs, in the following we show only the Vs models. For offshore locations, a water layer is placed above the sedimentary layer, with the thickness taken from the ETOPO1 global relief model (Amante & Eakins 2009) with Vs = 0 km s^{-1}, Vp = 1.45 km s^{-1} and density = 1.02 g cm^{-3}.

Finally, the Q model is specified as follows. In the sediments and crust, the Q model is from AK135, in which Q_μ is 600 in the crust and 80 in the sediments. The crustal Q value is high enough that there is little physical dispersion in the crustal shear modulus. In the mantle, the Q_μ model is taken from the global model of Dalton & Ekström (2006). The physical dispersion correction follows Anderson & Kanamori (1977).

4.2 Prior constraints and distributions

Prior constraints are of two types. First, we consider only particular ranges of perturbations to the starting model at each point, which

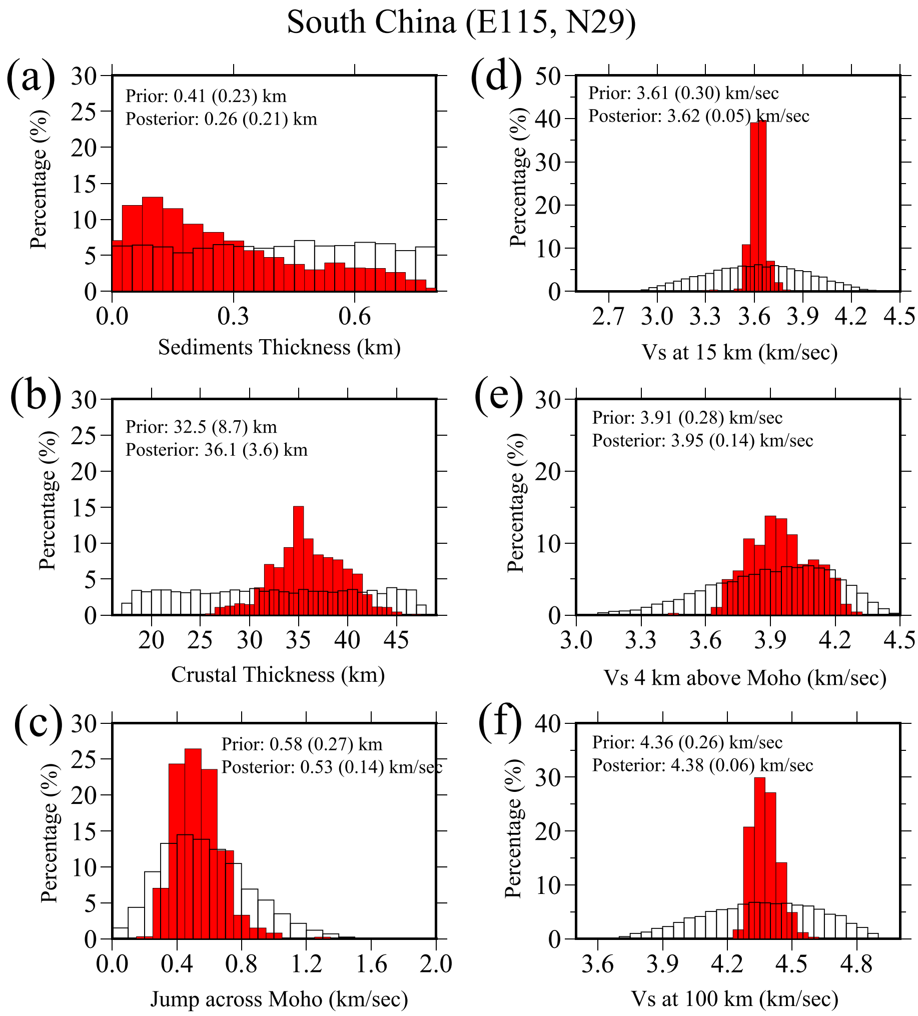

Figure 14. Examples of the prior and posterior distributions for several model variables at the location in South China identified by a star in Fig. 1(a), where the prior is shown with the white histogram and the posterior by the red histogram. (a) Sedimentary thickness, in km. (b) Total crustal thickness, in km. (c) Jump across Moho: Vs (4 km below Moho) – Vs (4 km above Moho), in km s^{-1}. (d) Vs at 15 km, in km s^{-1}. (e) Vs 4 km above Moho, in km s^{-1}. (f) Vs at 100 km, in km s^{-1}. The mean and standard deviation of both prior and posterior distributions are labelled on each panel, where the standard deviation appears in parentheses.

is a combination of the three models of Yang *et al.* (2012), Zhou *et al.* (2012), and Zheng *et al.* (2011). In the parts of our study region not covered by these three models, we start from the global model of Shapiro & Ritzwoller (2002). Consistent with our intent that this is a reference model, ranges of allowed model values are broad so that the standard deviation of the posterior distribution will reflect information from data more than prior constraints. For the sediments, we allow sedimentary thickness to range from 0 km to 200 per cent of the thickness of the starting model. If the starting model thickness is <0.4 km, we allow from 0 km to 0.8 km of sediments. Vs at the top and bottom of the sediments is allowed to change by ±1 km s^{-1}. If there are no sediments in the starting model at a particular location, we define the starting sedimentary model to possess 0.4 km of sediments with Vs at the top of the sediments equal to 1.5 km s^{-1} and at the bottom to 2.5 km s^{-1}. For the crystalline crust, we allow Vs to vary ±20 per cent relative to the starting model and crystalline crustal thickness to vary by ±15 km. For the mantle, we allow Vs to change by ±20 per cent relative to the starting model. Second, in addition we place three further constraints on the model and between model variables. (1) Vs <4.9 km s^{-1} at all depths in the model. (2) The jumps in Vs from the sediments to the crystalline crust and from the crust to the mantle are positive. (3) At some places we impose the constraint that Vs in the crust increases monotonically with depth and refer to this as the 'monotonicity constraint'. The use of cubic B-splines to represent seismic structure between discontinuities imposes a fourth implicit constraint that vertical variations between discontinuities are smooth. We see the application of these constraints as a hypothesis test such that we choose to introduce further structural complexities only where required by the data. As discussed shortly, the principal example of the release of a constraint is that Tibet must be freed from the crustal monotonicity constraint to fit our dispersion data. In particular, we release the constraint west of 110 °E longitude where surface elevation is higher than 2000 m.

Examples of prior distributions for several model variables are shown with the white histograms in Figs 14–16 corresponding to the same three locations in South China, Northeastern China, and Tibet for which the dispersion curves are shown in Fig. 7. The prior distributions for sedimentary and crustal thickness (panels a and b in each figure, respectively) are approximately uniform, whereas for the other variables they are not: (c) velocity jump across Moho: Vs(4 km below Moho) – Vs(4 km above Moho), (d) Vs at 15 km

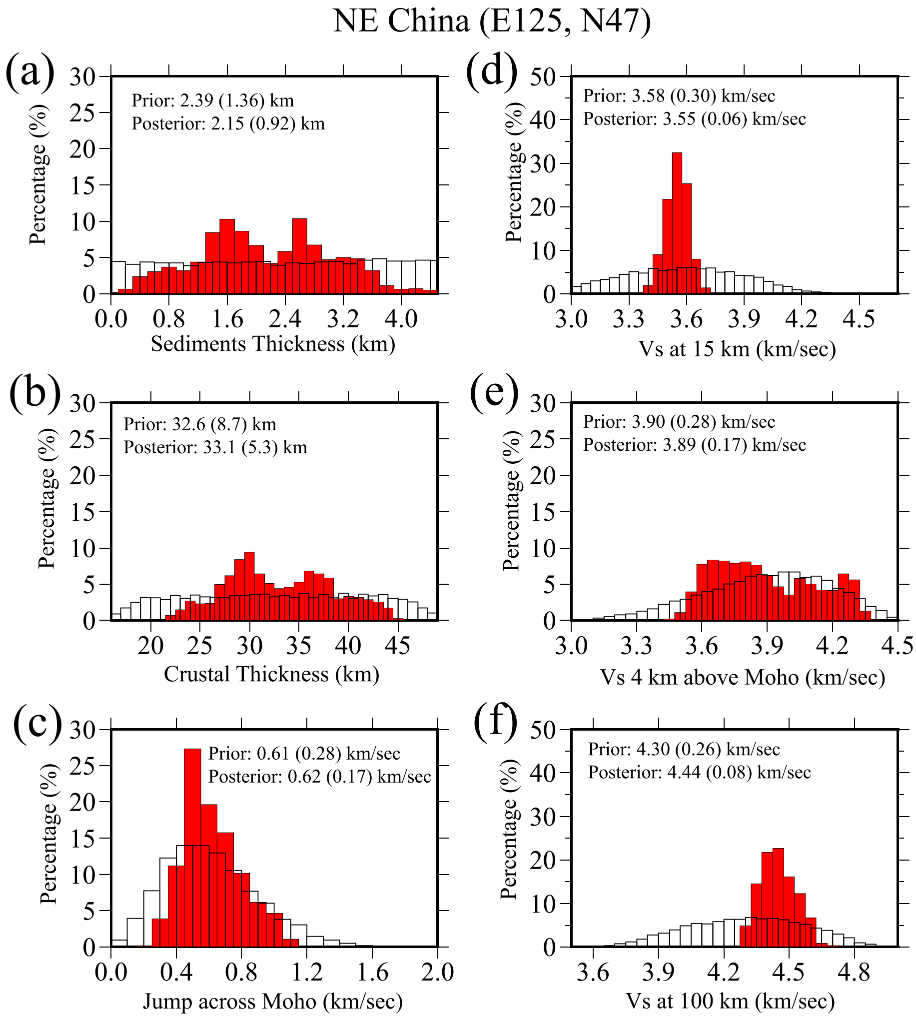

Figure 15. Similar to Fig. 13, but for the location in Northeast China identified by a star in Fig. 1(a).

depth, (e) Vs at 4 km above Moho, and (f) Vs at 100 km depth. The reason for the non-uniformity of the other prior distributions is that the other variables are constrained to co-vary with one another by the prior constraints. For example, the crustal monotonicity constraint ensures that Vs deeper in the crust is greater than at all shallower levels and the prior distributions for crustal velocities appear as skew Gaussian distributions.

4.3 Posterior distributions

Figs 14–16 superimpose the posterior marginal distribution on the prior distributions at locations in South China, Northeast China, and Tibet. To understand the posterior distributions it is necessary to recognize that surface waves do not strongly constrain the depths to internal interfaces or velocity jumps across them. Therefore, the distributions of sedimentary (panel a) and crustal (panel b) thicknesses as well as the velocity jump across Moho (panel c) at all three locations are quite broad. The single exception is in South China where the distribution of crustal thickness peaks relatively sharply near 35 km (Fig. 14b). In this case Rayleigh wave velocities, particularly the Airy phase on the group velocity curve, impose relatively strong constraints on crustal thickness because the structure at this point is simple and there are not strong trade-offs with, for example, sedimentary thickness and velocity. Because the jump across Moho generally is not well constrained, neither will Vs near the Moho be well constrained, which accounts for the fact that the posterior distributions at all three points are broad 4 km above Moho. However, within the crust and mantle well away from internal interfaces, the posterior distributions of Vs are quite sharp.

We summarize the posterior distributions with their means and standard deviations, and maps of these quantities are presented and discussed in Section 5. As we have discussed here, broad posterior distributions will produce a poorly determined mean with a large standard deviation. Generally speaking, the standard deviations of the posterior distributions in our model are relatively larger for depths near the Moho than for shear waves speeds within the crust and mantle. Thus, inspection of the posterior distributions reveals that inversions based on surface wave dispersion data alone constrain shear wave speeds relatively well within the interior of the crust and uppermost mantle and the depths and nature of the interfaces are much more poorly determined. This can be seen more clearly in plots of the envelope of accepted models such as those presented in Fig. 17, which are for the same three locations shown in Fig. 10 and Figs 14–16 in Tibet, South China, and Northeast China. The envelopes of these models broaden near the surface and near the Moho due to trade-offs between model variables, but reduce appreciably within the crust and uppermost mantle. The exception is in Tibet where the envelope does not narrow in the mantle. This reflects the fact that dispersion data in Tibet extend only up to 50 s

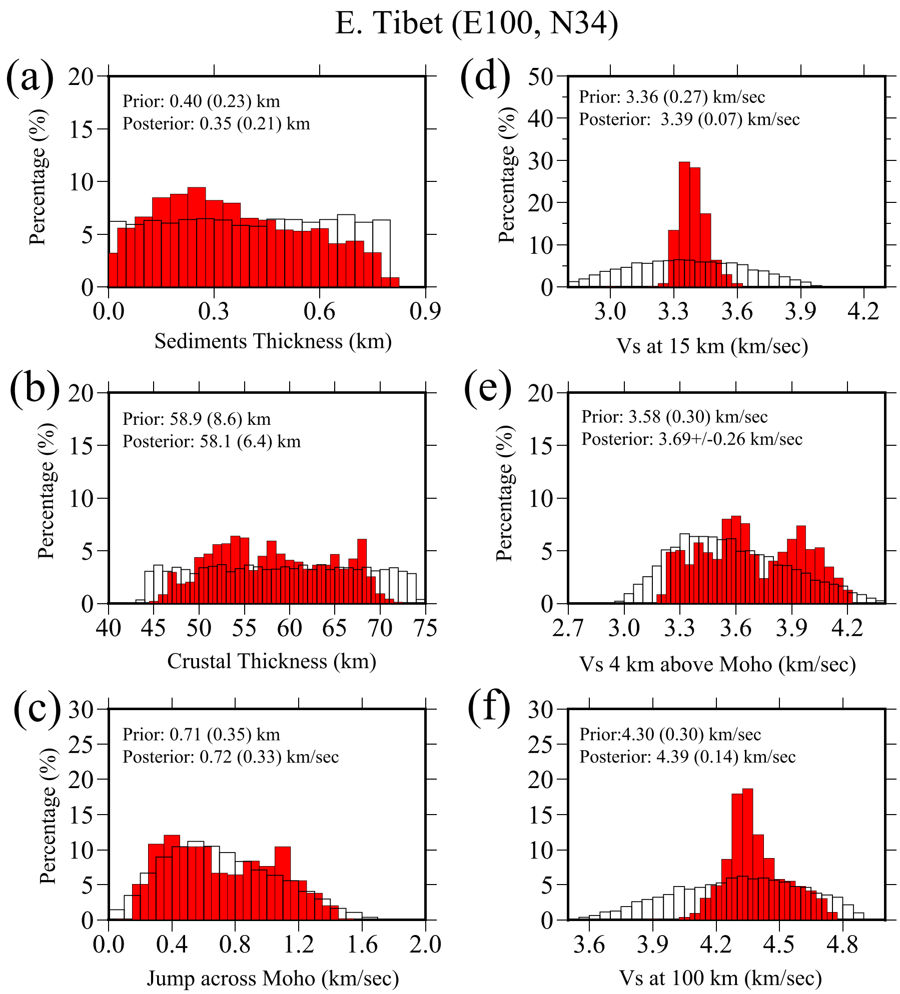

Figure 16. Similar to Figs 13 and 15, but for the location in Tibet identified by a star in Fig. 1(a).

period, where there is still a strong but unresolved sensitivity to both crustal thickness (given the deep Moho beneath Tibet) and mantle shear wave speeds.

Examples of the fit to the input dispersion curves by the mean of the posterior distribution at the same three locations are presented in Fig. 10. Misfit is defined as the square root of the reduced χ^2 value at each location as follows:

$$\text{Misfit} = \left[\frac{1}{N}\sum_{i=1}^{N}\frac{(d_i - p_i)^2}{\sigma_i^2}\right]^{1/2}, \tag{2}$$

where d_{i} is an observed Rayleigh wave phase or group speed, p_{i} is the corresponding model predicted value, σ_{i} is the one standard deviation uncertainty in the phase or group speed, i is an index that ranges over the discrete phase and group speed measurements, and N is the number of these measurements. A misfit of one standard deviation on average would result in a Misfit estimate equal to about 1. For the Northeast China location in Fig. 10, Misfit is 0.76 consistent with a misfit of about 1 standard deviation. The Misfit at the South China location (Fig. 10b), however, is 0.43, which may indicate that uncertainties are overestimated at this point or that the model is overparametrized somewhat. Fig. 10(a) illustrates that the Misfit at the location in Tibet depends on how we parametrize the model. The dispersion curves predicted from the crustal model produced with the monotonicity constraint are shown with the dashed lines in Fig. 10(a), which generates a Misfit of 2.01. With the crustal monotonicity constraint imposed in Tibet, we misfit the data badly. However, if we release this constraint we are able to fit the data well, generating a Misfit of 0.81 at the location in Fig. 10(a). The reason is that Tibet possesses a low-velocity zone in the central crust (e.g. Yang *et al.* 2012; Xie *et al.* 2013; Jiang *et al.* 2014; Deng *et al.* 2015), which is required to fit the dispersion data. Thus, as mentioned above, we release the crustal monotonicity constraint in Tibet west of 110° East longitude wherever surface elevation is greater than 2000 m.

The Misfit map computed using the mean model in the posterior distribution at each location is presented in Fig. 18(a) and the distribution of Misfit is presented by the histogram in Fig. 18(b). Misfit is typically less than 1 except in far western Tibet, in the Tarim basin west of a longitude of 95°E, and in the Sea of Japan. These are the areas where we have the fewest stations and the higher Misfit values probably indicate that data uncertainties are somewhat too small in these regions. However, across most of the region of study, the level of Misfit is consistent with the conclusion that data uncertainties are approximately correct and that the model generally possesses an appropriate number of degrees of freedom.

5 RESULTS

The model we present here (i.e. the mean of the posterior distribution) together with its attendant uncertainties (i.e. the

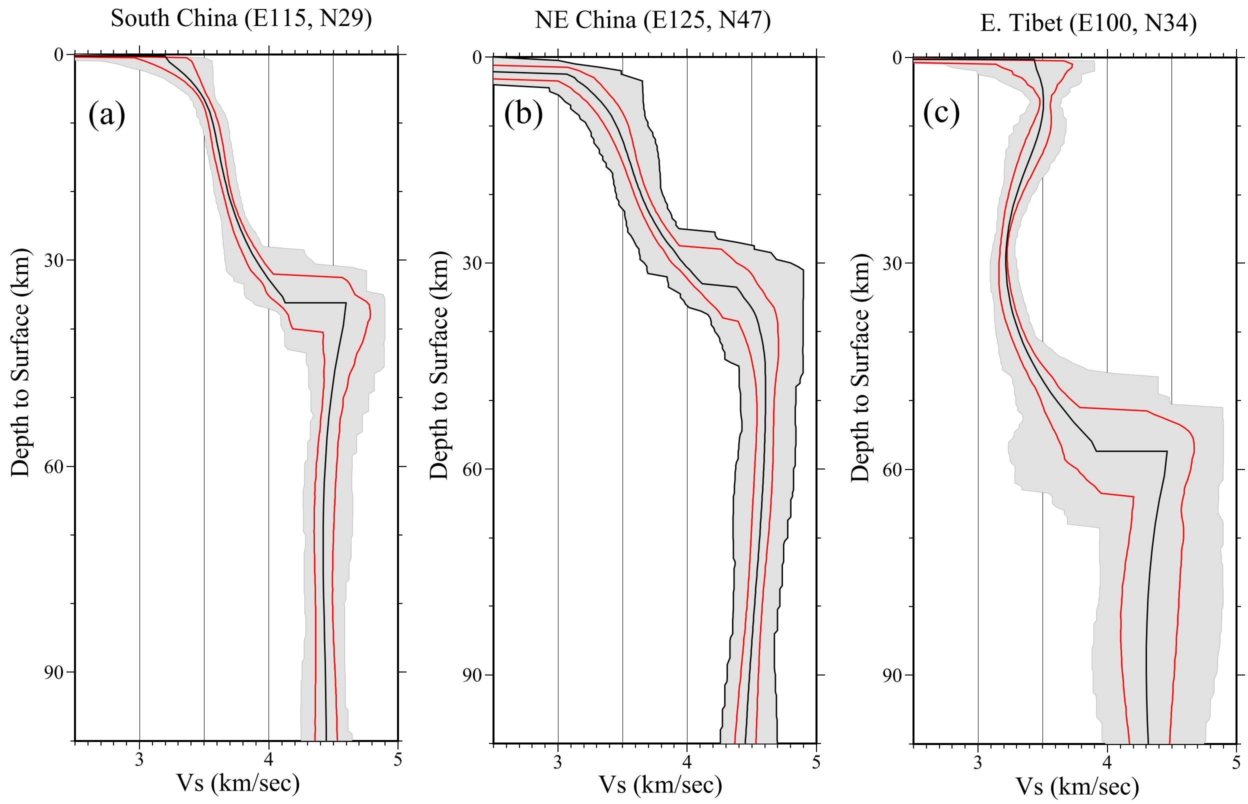

Figure 17. Vertical envelope (grey shaded region) formed by the full set of accepted shear velocity models in the posterior distribution for the same three locations for which dispersion measurements are shown in Fig. 10, identified by stars in Fig. 1(a). The black lines identify the mean of each distribution (from which the solid curves in Fig. 10 are computed) and the red lines identify the one standard deviation perturbations in the posterior distributions.

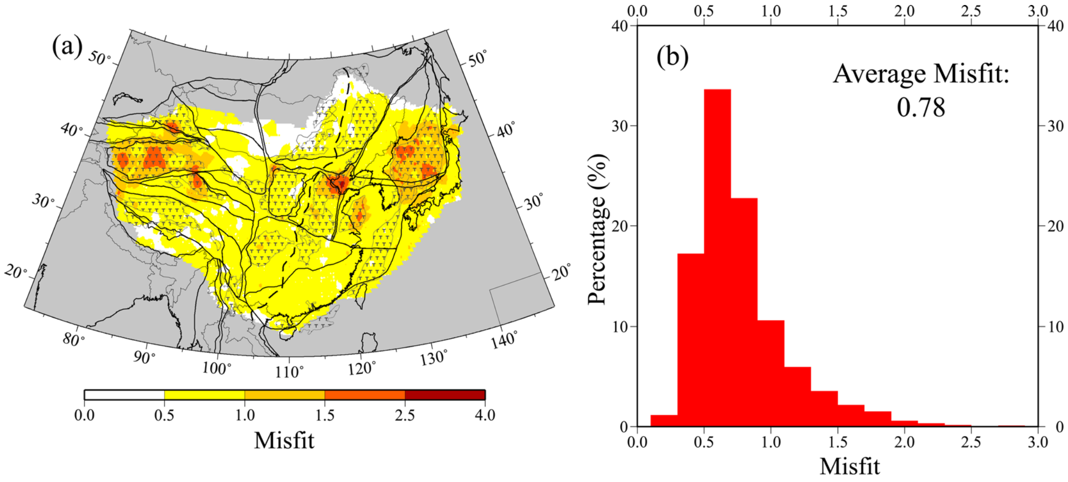

Figure 18. (a) Total Misfit, defined by eq. (2), between the observed Rayleigh wave dispersion curves and the curves computed from the mean of the posterior distribution at each point. (Misfit is defined as the square root of the reduced χ^2 value.) (b) Histogram of Total Misfit. Average Misfit is about 0.8.

standard deviation of the posterior distribution) are available via the IRIS Earth Model Collaboration (Trabant *et al.* 2012) at: http://ds.iris.edu/ds/products/emc/. At the time of publication, the model, uncertainties and the dispersion maps are also available via the CU-Boulder web site at: http://ciei.colorado.edu/Models and http://ciei.colorado.edu/DispMaps.

5.1 Interpreting the model and model uncertainties

We apply a Bayesian Monte Carlo inversion procedure to produce posterior distributions of models at each node on a 0.5° × 0.5° grid across the region of study. We summarize these distributions at each node and depth with the mean, $\bar{m}$, and standard deviation, σ_m. The resulting depth dependent interpolated pair ($\bar{m}$, σ_m) across the region of study forms our 3-D model.

The means and standard deviations of the posterior distributions across the study region are displayed at a variety of depths within the crust and uppermost mantle and for crustal thickness in Figs 19–21. Information about crustal shear wave speeds is found in Fig. 19, crustal thickness in Fig. 21, and mantle shear wave speeds in Fig. 20. Vertical transects through the model are identified in Fig. 21(a) and shown in Fig. 22.

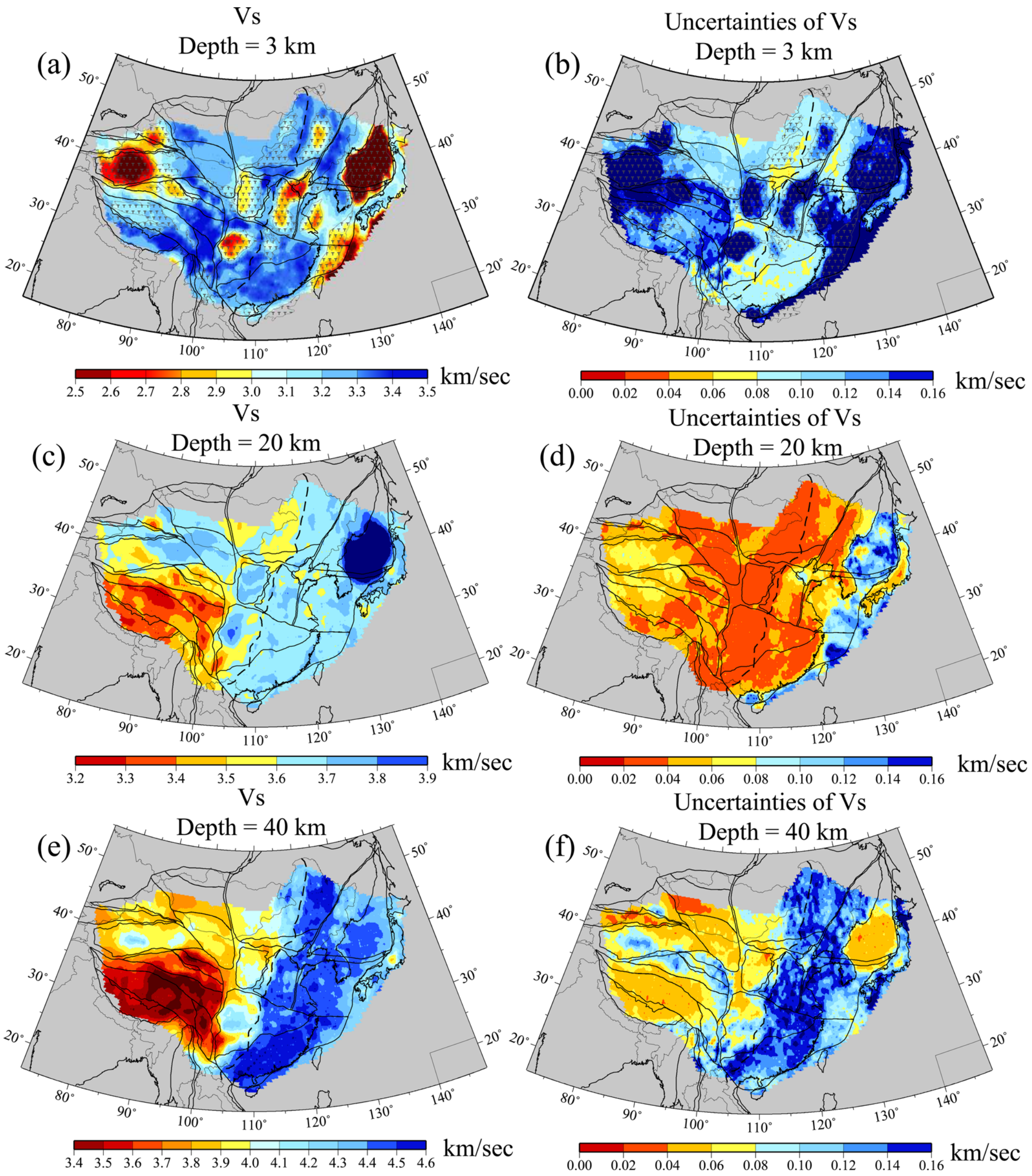

Figure 19. The estimated shear velocity model and uncertainties at three depths: (a,b) 3 km, (c,d) 20 km and (e,f) 40 km. The model and its uncertainty are the mean and standard deviation, respectively, of the posterior distribution averaged within ±3 km of each depth. The model and its standard deviation are presented in km s^{-1}.

Shen & Ritzwoller (2016) argue that the standard deviation of the posterior distribution, σ_m, is not an ideal estimate of absolute model uncertainty, but it provides useful information about relative uncertainty. It is too large to represent the effect of random error and does not include an estimate of systematic error. A better estimate of random error on the model is the standard deviation of the mean of the posterior distribution, $\sigma_{\bar{m}}$. Shen and Ritzwoller argue that this statistic provides a better estimate of the fluctuations observed in the 3D model and more accurately reflects the impact on model variables of data uncertainties. They argue that, on average, $\sigma_{\bar{m}}$ can be estimated by scaling σ_m by about 1/4. Thus, in the results that follow, the uncertainty estimates presented in Figs 19–21 should be considered relative errors. To estimate absolute effects of random errors on the model, the results in these figures should be multiplied by about 0.25.

5.2 Crustal structure and uncertainties

In the shallow crust, the pattern of shear wave speeds between the free surface and 6 km depth, presented as 3 km in Fig. 19(a), is dominated by the existence or absence of sediments such that the major sedimentary basins across China and offshore appear as slow anomalies. These include the Junggar, Tarim, Sichuan, Jianghan, North China (Bohaiwan, Taikang Hefei), and Songliao basins onshore along with basins offshore (East China Sea, Subei Yellow Sea, Tsushima). As illustrated by Figs 14–16, surface wave dispersion alone does not constrain sedimentary characteristics uniquely; for example, there is a strong trade-off between the thickness and average shear wave speeds within the sedimentary column as well as with the shear wave speeds in the shallow part of the underlying crystalline crust. For this reason, we do not present maps of sedimentary thickness, but rather show the shear wave speed averaged in

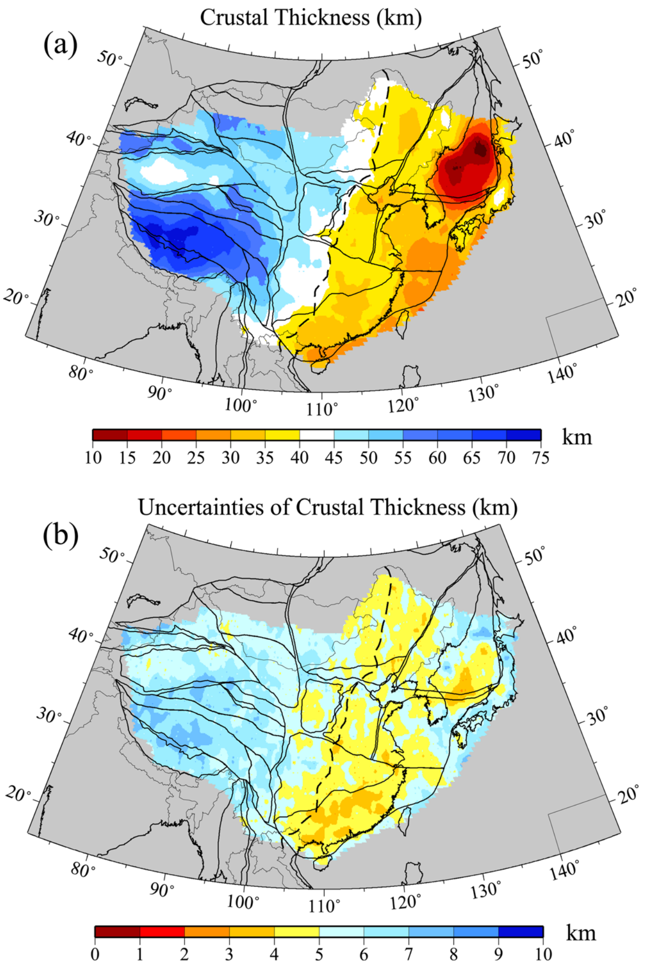

Figure 20. Estimated (a) crustal thickness and (b) its uncertainty, where crustal thickness is the mean of the posterior distribution at each location and uncertainty is its standard deviation, both presented in km.

the top 6 km near the surface of our model. The average shear wave speed offshore includes the water layer in which shear wave speed is zero, which is why the average is low offshore particularly in the Sea of Japan where water depth is largest. Moreover, our model of the vertical variation of Vs with depth within the sediments is crude, being a linear function of depth. The diagenesis and metamorphism of sediments produce a more complicated depth dependence than such a simple model. Our model of sediments exists for the most part, therefore, to capture the effects of sedimentary basins on surface wave propagation so that deeper structures can be revealed reliably. Better constraints on sedimentary structure require the introduction of other types of data such as receiver functions or Rayleigh wave H/V measurements (e.g. Deng *et al.* 2015; Kang *et al.* 2016).

In the middle crust, shear wave speeds near 20 km depth are presented in Fig. 19(c). Mid-crustal Vs in Tibet is anomalously low due to the well-known low-velocity zone that characterizes the Tibetan crust (e.g. Cotte *et al.* 1999; Rapine *et al.* 2003; Shapiro *et al.* 2004; Guo *et al.* 2009; Yang *et al.* 2012; Xie *et al.* 2013), which has been taken as evidence for the presence of partial melt (e.g. Kind *et al.* 1996; Caldwell *et al.* 2009; Chen *et al.* 2014; Hacker *et al.* 2014). The middle crust across East China is fairly homogeneous, with the exception of higher Vs beneath the Sichuan basin and Ordos block and lower Vs beneath the Yangtze craton south of the Sichuan basin and beneath the Tianshan terrane and Outer Mongolia (e.g. Tamtsag Halar and Erlian basins). Offshore, Vs near 20 km depth beneath the Sea of Japan is high because this depth is in the mantle due to the thin oceanic crust.

In the lower crust, a strong east-west dichotomy is observed at 40 km depth in Fig. 19(e). This is because the crust thins eastwards beneath China and crosses the 40 km isoline near the North-South gravity lineament (dashed line in Figs 19–21). West of the North-South gravity lineament, 40 km depth lies in the crust. In this region outside of Tibet, for example beneath the Sichuan basin, the Ordos block, and the Tarim basin, 40 km lies in the very deep and presumably mafic lower crust with shear wave speeds above 4.0 km s^{-1}. In contrast, beneath Tibet 40 km lies in the middle crust, which has much lower shear wave speeds. Much of the Songpan-Ganzi terrane at this depth has Vs $<$3.5 km s^{-1}. East of the North-South gravity lineament, 40 km depth lies in the mantle and Vs is relatively homogeneous across this region.

Crustal thickness estimates are presented in Fig. 20. On average, the crust thins eastward. As just discussed, the North-South gravity lineament marks the approximate locus of points for 40 km thick crust. The crust is thickest in central Tibet, where we estimate maximum crustal thickness above 65 km, and is thinnest beneath the Sea of Japan with crust less than 15 km thick.

Uncertainties in crustal shear velocities and crustal thickness, defined as the standard deviation of the posterior distribution at each point, are also presented in Figs 19 and 20. Uncertainties at shallow depths (Fig. 19b) are highest beneath sedimentary basins due to structural trade-offs, as already discussed, and in the western parts of our model where station density is lowest (e.g. longitudes west of 95°E). In the middle crust (Fig. 19d), on the continent uncertainties are much smaller due to the separation of 20 km depth from crustal interfaces, notably the sediment-crystalline crust boundary and the Moho. This is mitigated somewhat in regions with thick sediments (e.g. Songliao basin, North China basins). Uncertainties are also relatively large in western Tibet and beneath the Tarim basin due to rarified station coverage. Offshore, however, uncertainties are much larger at this depth because the crust is thinner and the Moho approaches 20 km in many locations. At 40 km depth, the magnitude of the uncertainties (Fig. 19f) is also controlled by the proximity to the Moho. East of the North-South gravity lineament uncertainties are large and west of it they are smaller, except near the periphery of Tibet and beneath the Tarim basins where the Moho approaches this depth from above. In contrast, uncertainties beneath the Sea of Japan are quite small. Uncertainties in crustal thickness (Fig. 20b) also scale with crustal thickness so that they are largest beneath Tibet and smallest beneath the Sea of Japan and the South China block. This is largely due to the band-limited content of the data we use. Beneath Tibet, for example, the data only extend to 50 s period, which is not long enough to constrain mantle Vs well and reduce its trade-off with Moho depth.

5.3 Mantle structure and uncertainties

At 60 km depth (Fig. 21a), which is predominantly in the mantle except beneath parts of Tibet, the highest Vs values occur beneath the major basins including part of the Songliao, Sichuan, and Tarim basins and the Ordos block where Vs $>$ 4.5 km s^{-1}. Beneath Tibet, the crust is so thick that it envelopes 60 km, and average lower crustal Vs is about 3.7 km s^{-1}. Uncertainties at this depth (Fig. 21b) also reflect the relative proximity to the nearest discontinuity, which is the Moho, and are higher where the crust is thicker. East of the North-South gravity lineament, where Moho lies above 40 km depth, uncertainties average about 70 m s^{-1}, which is about 1.5 per cent.

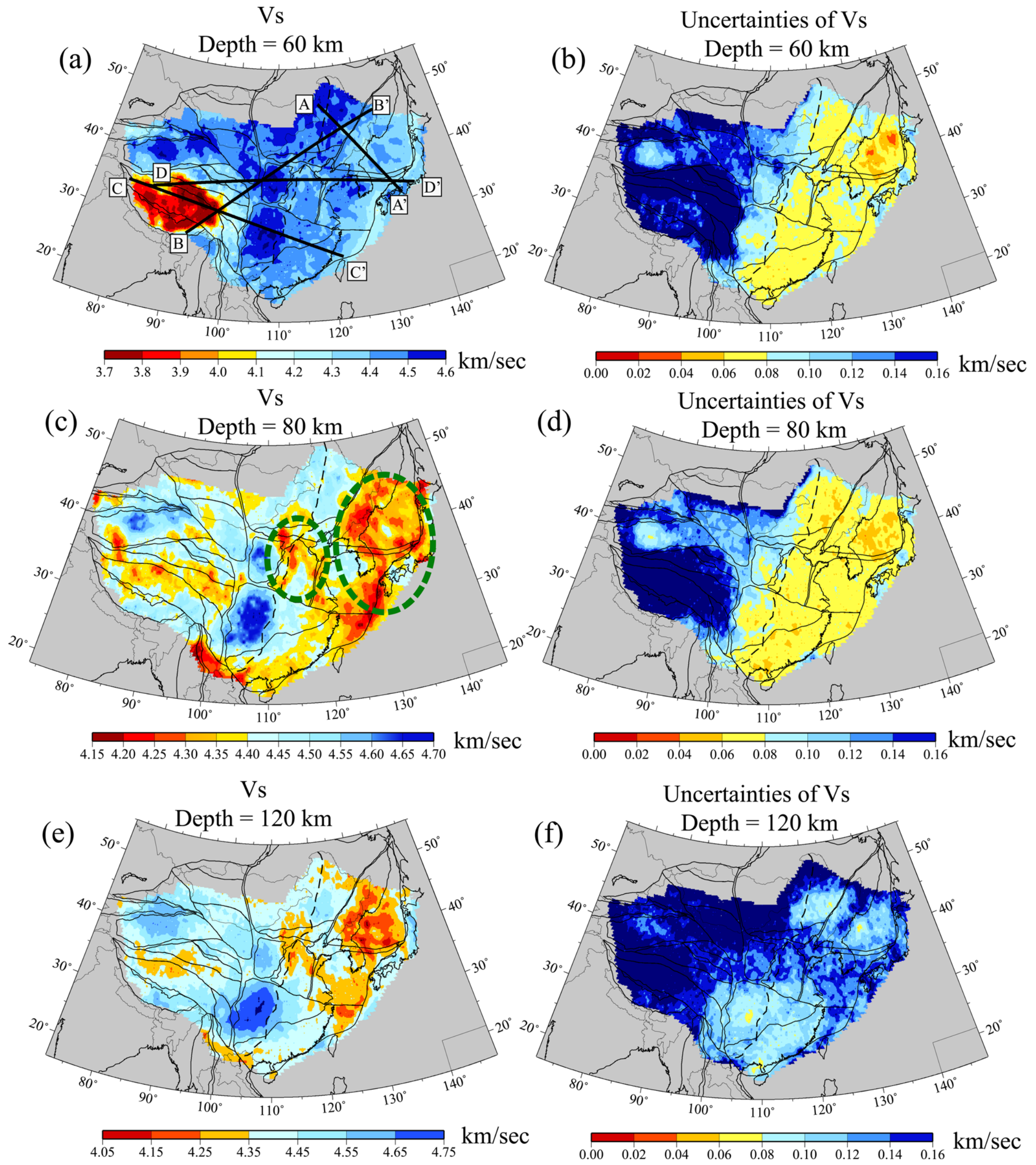

Figure 21. Similar to Fig. 19, but at three different depths: 60, 80 and 120 km. Two anomalies in the mantle are highlighted in (b): the so-called horseshoe shaped anomaly (small green oval) and the Y-shaped anomaly (large green oval) referred to by Zheng *et al.* (2011). Locations of the vertical transects displayed in Fig. 22 are shown in (a).

In many respects, the model is similar at depths of 80 and 120 km (Figs 21c and e), and the content of the model at these depths is discussed in the following paragraphs. The geographical distributions of uncertainties at 80 and 120 km are similar (Figs 21d and f). However, uncertainties are larger at 120 km because our band-limited dispersion measurements begin to lose resolution below 100 km. The exception to this is beneath South China and Northeast China where we have earthquake derived dispersion measurements, which illustrates why we have taken pains to introduce these measurements. Beneath the Tibetan Plateau the uncertainties are high at 60 and 80 km mainly because the shear wave velocities at these depths trade off with the Moho depth, which is ∼60–70 km in this area.

At 80 km depth, high-velocity anomalies at this depth underlie those principal sedimentary basins (Tarim, Songliao, Jianghan, Taikang Hefei, Sichuan) and the Ordos block. In addition there are high-velocity anomalies beneath the Lhasa terrane in southern Tibet, the Greater Xing'an Range, and the Yellow Sea. The high-velocity anomaly beneath the Sichuan basin extends well outside the basin, and occupies much of the western Yangtze craton, so we will refer to it as the western Yangtze craton. The highest velocities underlie the Tarim basin, the western Yangtze craton, and the Ordos block. We believe these structures reflect the ancient origin of these tectonic features and contrast with the weaker positive velocity anomaly that underlies the next largest basin in our study region, the Songliao basin, which is believed to have formed much more recently (Tian *et al.* 1992; Liu *et al.* 2001).

Low-velocity anomalies include low wave speeds beneath northern Tibet that have reported by previous researchers (e.g. Shapiro *et al.* 2004; Yang *et al.* 2012; Xie *et al.* 2013), an anomaly related to Datong volcano merging into a 'horseshoe shaped' or 'crescent shaped' (small green dashed oval in Fig. 21c) anomaly that outlines the northern part of the North China Plain, and a 'Y-shaped' (large

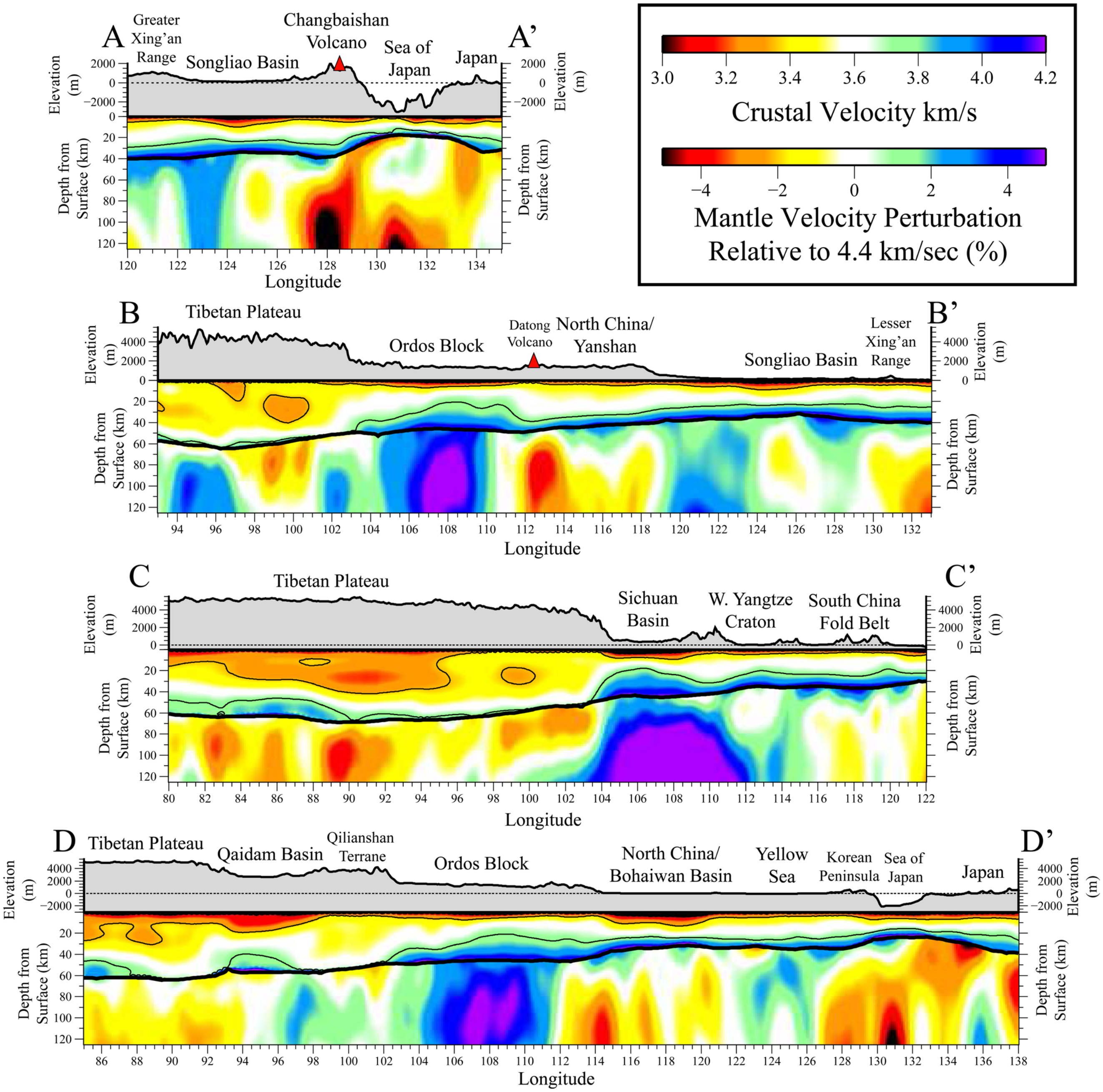

Figure 22. Vertical transects running along the four profiles (A–A′, B–B′, C–C′, D–D′) identified in Fig. 21a. Crustal velocities are presented in km s^{-1} and mantle velocities are expressed as the perturbation to 4.4 km s^{-1} presented in percent. The locations of geological and tectonic features are identified above each transect along with surface topography. Transects are vertically exaggerated but horizontal distances are equally scaled between them.

green dashed oval in Fig. 21c) anomaly that encompasses both near coastal areas of Northeast China, North Korea, and South Korea as well as more seaward areas along the Ryukyu subduction zone and the eastern periphery of the Sea of Japan. The 'horseshoe shaped' and 'Y-shaped' anomalies were discussed in some detail by Zheng *et al.* (2011), but are now imaged more sharply due to the introduction of data from the Korean Seismic Network and the NECESS array.

The low-velocity anomaly in the uppermost mantle beneath northern Tibet has been interpreted as a remnant of a gravitational instability that caused the foundering of unstable lithosphere (England *et al.* 1988; Kosarev *et al.* 1999). The horseshoe shaped anomaly has also been interpreted to result from the broadly hypothesized delamination (or some similar process) of the lithosphere beneath the North China craton by Zheng *et al.* (2011). Zheng *et al.* (2011) interpret the Y-shaped anomaly are deriving from upwelling fluids derived from the subducting slab beneath and adjacent to the Sea of Japan. The recent P-wave tomography study of Tang *et al.* (2014) images a similar anomaly in the mantle but interprets it as a deep seated upwelling that penetrates through the slab from the lower mantle. The lack of long-period surface wave measurements in Tibet diminishes the quality of the 3-D model at depths greater than 100 km, which calls for future refinements that incorporate surface wave studies using earthquakes.

5.4 Vertical transects through the model

Upper mantle structure and perhaps to a lesser extent crustal structure can be seen in an illuminating way with vertical transects such as those identified in Fig. 21(a) and presented in Fig. 22. Transect A–A′ goes through Northeast China from the Greater Xing'an Range, through the Songliao basin, passing beneath Changbaishan volcano, and then through the southern Sea of Japan to terminate near Japan. The uppermost mantle beneath the Great Xi'an Range and the western Songliao basin is fast, as is the shallow lithosphere beneath the Sea of Japan. Beneath the Changbaishan the mantle is quite slow, however, and upper-mantle low-velocity anomalies bracket the Sea of Japan as part of the so-called 'Y-shaped' anomaly identified by Zheng *et al.* (2011). The crust can be seen to thin sharply beneath the Sea of Japan and slightly beneath the Songliao basin.

The other vertical transects shown in Fig. 22 are much longer than transect A–A′. Transect B–B′ extends from Tibet, through the Ordos block, passing beneath Datong volcano and the Yangshan Foldbelt, and then through the Songliao basin to terminate in the Lesser Xi'an Range east of the basin. The most prominent mantle anomalies are the thick, high-velocity lithosphere that underlies the Ordos block and the very low velocity anomaly that underlies Datong volcano. The difference between the high-velocity upper mantle beneath southern Tibet and the lower velocities beneath northern Tibet is also apparent. This profile also captures the difference between the fast western and slow eastern Songliao basin. Transect B–B′ also shows low-velocity middle crust in northern Tibet, very fast lower crust beneath the Ordos, crustal thickening beneath Tibet and thinning beneath the Songliao basin.

Transects C–C′ and D–D′ also start in Tibet on the West. C–C′ extends through the western Yangtze craton, including the Sichuan basin, through the South China block, and terminates off the coast in the South China Sea north of Taiwan. In Tibet, this transect goes exclusive through the low-velocity uppermost mantle of Northern Tibet. Low velocities in the mantle also underlie the South China fold belt below 60 km depth, characteristic of thin lithosphere in this region. Most prominently, however, are the high velocities beneath the western Yangtze craton, which is the strongest mantle high-velocity anomaly in the study region. Crustal features include the mid-crustal low-velocity zone in Tibet, the thick sediments of the Sichuan basin, and exceptionally high-velocity lower crust in the western Yangtze craton. Transect D–D′ emerges from Tibet and goes through the Qaidam basin, the Qilianshan block, the Ordos block, and the northern reaches of the North China Plain, and then extends through the Yellow Sea, the Korean Peninsula, and the southernmost Sea of Japan before terminating near Japan. Several of the features seen in this transect are mentioned for previously discussed transects. In addition to the Ordos block, particularly prominent features in this transect include thick sediments beneath the Qaidam and North China basins, thin lithosphere beneath the North China Plain, and the low-velocity anomalies that bracket the Sea of Japan.

6 CONCLUSIONS

The purpose of this study is to produce a reference model for the crust and uppermost mantle beneath the study region, which encompasses all of China and extends eastwards into the marginal seas, through North and South Korea, to Japan. By 'reference model' we mean a seismic model that is designed to be used by researchers other than its authors. In our view, a reference model has three necessary characteristics. (1) Uncertainties are estimated for the model variables. (2) The data on which the model is based are available to other researchers. (3) The model itself and uncertainties are available to other researchers. In addition, it is advantageous if the reference model is based on a uniform quality control procedure applied to all observables and if prior constraints are clearly described and also preferably broad.

Using data from more than 2000 seismic stations taken from multiple networks arrayed across China (CEArray, China Array, NECESS, PASSCAL, GSN) and surrounding regions (Korean Seismic Network, F-Net, KNET) we perform ambient noise Rayleigh wave tomography across the entire region of study and earthquake tomography across parts of South China and Northeast China. The same quality control procedures are applied to all ambient noise data and all earthquake data. We produce isotropic Rayleigh wave group and phase speed maps with uncertainties from 8 to 50 s period across the entire region of study, which are extended to 70 s period where earthquake tomography is performed. In producing the isotropic maps, we also generate maps of azimuthal anisotropy to reduce potential anisotropic bias. These isotropic maps and the associated uncertainties are the basis for the 3-D model.

The 3-D model is produced using a Bayesian Monte Carlo formalism on a 0.5° × 0.5° grid across the study area. The starting model for the inversion is compiled from the models described by Yang *et al.* (2012) for Tibet, Zheng *et al.* (2011) for North/Northeast China and environs, and Zhou *et al.* (2012) for South China and, where they do not exist, from the global model of Shapiro & Ritzwoller (2002). Because we seek to produce a model that will be useful to other researchers, we intentionally keep prior bounds on the model broad. Such uninformative priors result in posterior distributions that more strongly reflect information in the data than prior information, about which other researchers may differ from us. The principal exception is that we attempt to fit the data with a vertically smooth or simple model between interfaces at the base of the sediments and crust. We acknowledge that the earth may not be vertically smooth, but believe that inference of vertically rough structures, such as the introduction of more crustal interfaces, should be compelled by the data, particularly for a reference model. The most stringent constraint that we impose is the crustal 'monotonicity constraint', which ensures that Vs increases with depth in the crust. Due to the crustal low-velocity zone in the Tibetan middle crust (e.g. Shapiro & Ritzwoller 2002; Yang *et al.* 2012; Xie *et al.* 2013), our data cannot be fit in Tibet with this constraint; thus, we release it west of 110°E longitude where surface elevation is higher than 2000 m. Elsewhere in the study region the crustal monotonicity constraint has been applied.

We define the final model as the mean and standard deviation of the posterior distribution on a 0.5° × 0.5° grid from the surface to 150 km depth. The mean model fits the dispersion data at about one data standard deviation, on average, indicating that the model is not systematically over or underparametrized relative to the size of data uncertainties. Rayleigh wave dispersion, unfortunately, does not constrain internal interfaces well. Because our model is based on Rayleigh wave dispersion alone and prior information is broad, sedimentary and crustal thicknesses and related variables are not precisely determined: their posterior distributions encompass much of their prior distributions. In contrast, shear wave speeds between discontinuities in the crystalline crust and below the Moho in the uppermost mantle are well determined and compose most of the information content in our model. We follow Shen & Ritzwoller (2016) and interpret the standard deviation of the posterior distribution, referred to as model uncertainty here, as a measure of relative error. A better estimate for the absolute effect of random data errors would result from multiplying the standard deviation of the posterior distribution by about 0.25.

The features that appear in the model display great variety and considerable richness both in the crust and in the uppermost mantle. We highlight only five here. (1) The major sedimentary basins dominate structures that we see in the uppermost crust, particularly for the Songliao, Bohaiwan, Jianghan, Sichuan, Qaidam, and Tarim basins. (2) An anomalously low-velocity channel appears in the middle crust of the Tibetan Plateau, in contrast to relatively fast middle crust in eastern China. (3) The principal lower crustal anomalies are exceptionally high velocities beneath the sedimentary basins, most prominently beneath the Ordos Block. (4) Crustal thickness varies from less than 15 km beneath the Sea of Japan to more than 60 km beneath the Tibetan Plateau, and the 40 km crustal thickness boundary coincides approximately with the North-South Gravity Lineament dividing continental China into two distinct zones. (5) In the uppermost mantle, the most notable features are fast anomalies beneath the Sichuan basin and the Ordos Block and slow anomalies comprising the 'horse-shoe' shaped anomaly surrounding the North China Plain and the 'Y-shaped' anomaly bracketing the Sea of Japan. Relatively slow anomalies are observed beneath northern Tibet. The slow anomalies are related either to delamination/gravitational instability or the subduction of the Pacific Plate. Each of these features deserves further detailed discussion, which is beyond the scope of this paper.

We present the reference model as a basis for future research and see it as representing a first iterate. It is designed to be used as a basis for predicting waveform characteristics, such as surface and body wave amplitudes and traveltimes, and with the right interpretation to predict other kinds of data such as surface topography and gravity (e.g. Levandowski *et al.* 2014). Although the model reflects the content of an exceptionally large data set of inter-station surface wave dispersion measurements, the introduction of more and various types of data will bring it into closer coincidence with the earth. The joint inversions performed with receiver functions (Shen *et al.* 2013a,b; Deng *et al.* 2015) and Rayleigh wave ellipticity or H/V (Lin *et al.* 2012, 2014) are natural candidates for future refinements. For example, Deng *et al.* (2015) show that the joint inversion of the dispersion data we present here with receiver functions at a transect in northern Tibet requires the introduction of internal interfaces within the Tibetan middle crust as well as a double Moho, and reveals a step in Moho north of the Kunlun fault. Kang *et al.* (2016) assimilates our data and inverts them together with receiver functions and Rayleigh wave H/V ratio measurements from the NECESS Array experiment and observes an asymmetric Moho depth variation, thinning from the west to the east, beneath the Songliao basin, attributed to recent mantle upwelling beneath the Changbaishan Volcano. Both of these studies are at regional scales, but they present important directions for future refinements to this reference model. The assimilation of Love wave measurements is another natural direction for future research. In addition, the continued installation and movement of China Array, in particular, promise a wealth of new information on which to base future refinements and improvements to the reference model at much higher resolution.

ACKNOWLEDGEMENTS

The authors are grateful to two anonymous reviewers for insightful comments that helped to improve this paper and to Jiayi Xie at University of Colorado Boulder for helping produce Fig. 5. DK, JN, WW, YZ and LZ all had extended work visits to the University of Colorado during which aspects of this work were completed, and they thank the following funding agencies for supported their visits: Chinese Geological Survey, National Science Foundation of China (NSFC) and China Scholarship Council. Aspects of this research were supported by NSF grant EAR-1246925 at the University of Colorado at Boulder. The facilities of IRIS Data Services, and specifically the IRIS Data Management Center, were used for access to waveforms, related metadata and/or derived products used in this study. IRIS Data Services are funded through the Seismological Facilities for the Advancement of Geoscience and EarthScope (SAGE) Proposal of the National Science Foundation under Cooperative Agreement EAR-1261681. China Array waveform data and some of the CEA array waveform data were provided by the Data Management Center of the China National Seismic Network at the Institute of Geophysics and China Seismic Array Data Management Center at the Institute of Geophysics, China Earthquake Administration (Zheng *et al.* 2010a). The China Array Project was supported by China National Special Fund for Earthquake Scientific Research in Public Interest (201008011) and WW's contribution has been supported by NSFC grant 41374070. YZ's contribution has been supported by NSFC grants 41422401 and 41174086. YK acknowledges National Research Foundation of Korea Grant funded by the Korean Government (NRF-2014S1A2A2027609), and also acknowledges the National Earthquake Comprehensive Information System (NECIS) website (in Korean) for the data. This work utilized the Janus supercomputer, which is supported by the National Science Foundation (award number CNS-0821794), the University of Colorado at Boulder, the University of Colorado Denver and the National Center for Atmospheric Research. The Janus supercomputer is operated by the University of Colorado at Boulder.

REFERENCES

Acton, C.E., Priestley, K., Gaur, V.K. & Rai, S.S., 2010. Group velocity tomography of the Indo-Eurasian collision zone, *J. geophys. Res.,* **115,** B12335, doi:10.1029/2009JB007021.

Amante, C. & Eakins, B.W., 2009. ETOPO1 1 Arc-Minute Global Relief Model: Procedures, Data Sources and Analysis. *NOAA Technical Memorandum NESDIS NGDC-24*. National Geophysical Data Center, *NOAA,* doi:10.7289/V5C8276M

Bao, X., Song, X., Xu, M., Wang, L., Sun, X., Mi, N. & Li, H., 2013. Crust and upper mantle structure of the North China Craton and the NE Tibetan Plateau and its tectonic implications, *Earth planet. Sci. Lett.,* **369,** 129–137.

Bao, X., Song, X. & Li, J., 2015. High-resolution lithospheric structure beneath Mainland China from ambient noise and earthquake surface-wave tomography, *Earth planet. Sci. Lett.,* **417,** 132–141.

Barmin, M.P., Ritzwoller, M.H. & Levshin, A.L., 2001. A fast and reliable method for surface wave tomography, *Pure appl. Geophys.,* **158**(8), 1351–1375.

Bensen, G.D., Ritzwoller, M.H., Barmin, M.P., Levshin, A.L., Lin, F., Moschetti, M.P., Shapiro, N.M. & Yang, Y., 2007. Processing seismic ambient noise data to obtain reliable broad-band surface wave dispersion measurements, *Geophys. J. Int.,* **169,** 1239–1260.

Brocher, T.M., 2005. Empirical relations between elastic wavespeeds and density in the Earth's crust, *Bull. seism. Soc. Am.,* **95**(6), 2081–2092.

Caldwell, W.B., Klemperer, S.L., Rai, S.S. & Lawrence, J.F., 2009. Partial melt in the the upper-mantle crust of the northwest Himalaya revealed by Rayleigh wave dispersion, *Tectonophysics,* **477,** 58–65.

Chen, M., Huang, H., Yao, H., Hilst, R. & Niu, F., 2014. Low wave speed zones in the crust beneath SE Tibet revealed by ambient noise adjoint tomography, *Geophys. Res. Lett.,* **41**(2), 334–340.

Cotte, N., Pederson, H., Campillo, M., Mars, J., Ni, J.F., Kind, R., Sondvol, E. & Zhao, W., 1999. Determination of the crustal structure in sourthern

Tibet by dispersion and amplitude analysis of Rayleigh waves, *Geophys. J. Int.,* **138,** 809–819.

Dalton, C.A. & Ekström, G., 2006. Global models of surface-wave attenuation, *J. geophys. Res.,* **111,** B05317, doi:10.1029/2005JB003997.

Deng, Y., Shen, W., Xu, T. & Ritzwoller, M.H., 2015. Crustal layering in northeastern Tibet: A case study based on joint inversion of receiver functions and surface wave dispersion, *Geophys. J. Int*., **203,** 692–706.

England, P.C., Houseman, G.A., Osmaston, M.F. & Ghosh, S., 1988. The mechanics of the Tibetan Plateau [and discussion], *Phil. Trans. R. Soc. A,* **326**(1589), 301–320.

Guo, Z., Gao, X., Yao, H., Li, J. & Wang, W., 2009. Midcrustal low-velocity layer beneath the central Himalaya and southern Tibet revealed by ambient noise array tomography, *Geochem. Geophys. Geosyst.,* **10**(5), Q05007, doi:10.1029/2009GC002458.

Guo, Z., Gao, X., Wang, W. & Yao, Z., 2012. Upper-and mid-crustal radial anisotropy beneath the central Himalaya and southern Tibet from seismic ambient noise tomography, *Geophys. J. Int.,* **189**(2), 1169–1182.

Guo, Z., Chen, Y.J., Ning, J., Feng, Y., Grand, S.P., Niu, F. & Ni, J., 2015. High resolution 3-D crustal structure beneath NE China from joint inversion of ambient noise and receiver functions using NECESSArray data, *Earth planet. Sci. Lett.,* **416,** 1–11.

Hacker, B.R. & Abers, G.A., 2004. Subduction Factory 3: an excel worksheet and macro for calculating the densities, seismic wave speeds, and H2O contents of minerals and rocks at pressure and temperature, *Geochem. Geophys. Geosyst.,* **5,** Q01005, doi:10.1029/2003GC000614.

Hacker, B.R., Ritzwoller, M.H. & Xie, J., 2014. Partially melted, mica-bearing crust in Central Tibet, *Tectonics,* **33**(7), 1408–1424.

Herrmann, R.B., 2013. Computer programs in seismology: an evolving tool for instruction and research, *Seismol. Res. Lett.,* **84,** 1081–1088.

Huang, H., Yao, H. & van der Hilst, R.D., 2010. Radial anisotropy in the crust of SE Tibet and SW China from ambient noise interferometry, *Geophys. Res. Lett.,* **37**(21), doi:10.1029/2010GL044981.

Huang, Z., Su, W., Peng, Y., Zheng, Y. & Li, H., 2003. Rayleigh wave tomography of China and adjacent regions, *J. geophys. Res.,* **108**(B2), 2073, doi:10.1029/2001JB001696.

Huang, Z., Li, H., Zheng, Y. & Peng, Y., 2009. The lithosphere of North China Craton from surface wave tomography, *Earth planet. Sci. Lett.,* **288**(1), 164–173.

Jiang, C., Yang, Y. & Zheng, Y., 2014. Penetration of mid-crustal low velocity zone across the Kunlun Fault in the NE Tibetan Plateau revealed by ambient noise tomography, *Earth planet. Sci. Lett.,* **406,** 1–92.

Jiang, M., Zhou, S., Sandvol, E., Chen, X., Liang, X., John Chen, Y. & Fan, W., 2011. 3-D lithospheric structure beneath southern Tibet from Rayleigh-wave tomography with a 2-D seismic array, *Geophys. J. Int.,* **185,** 593–608.

Kanamori, H. & Anderson, D.L., 1977. Importance of physical dispersion in surface wave and free oscillation problems: review, *Rev. Geophys.,* **15**(1), 105–112.

Kang, D., Shen, W., Ning, J. & Ritzwoller, M.H., 2016. Crustal and uppermost mantle structure beneath northeastern China from joint inversion of receiver functions, Rayleigh wave dispersion, and Rayleigh wave ellipticity, *Geophys. J. Int.,* **204**(1), 215–235.

Karplus, M.S., Klemperer, S.L., Lawrence, J.F., Zhao, W., Mechie, J., Tilmann, F., Sandvol, E. & Ni, J., 2013. Ambient-noise tomography of north Tibet limits geological terrane signature to upper-middle crust, *Geophys. Res. Lett.,* **40**(5), 808–813.

Kawakatsu, H., Yamamoto, M., Kaneshima, S. & Ohkura, T., 2011. Comment on “A persistent localzed microseismic source near the Kyushu Island, Japan” by Xiangfang Zeng and Sidao Ni, *Geophys. Res. Lett.,* **38,** L17307, doi:10.1029/2011GL048584.

Kennett, B.L.N., Engdahl, E.R. & Buland, R., 1995. Constraints on seismic velocities in the Earth from travel times, *Geophys J. Int.,* **122,** 108–124

Kind, R., Ni, J., Zhao, W., Wu, J., Yuan, X., Zhao, L. & Hearn, T., 1996. Evidence from earthquake data for a partially molten crustal layer in southern Tibet, *Science,* **274**(5293), 1692–1694.

Kosarev, G., Kind, R., Sobolev, S.V., Yuan, X., Hanka, W. & Oreshin, S., 1999. Seismic evidence for a detached Indian lithospheric mantle beneath Tibet. *Science,* **283**(5406), 1306–1309.

Legendre, C.P., Deschamps, F., Zhao, L., Lebedev, S. & Chen, Q.F., 2014. Anisotropic Rayleigh wave phase velocity maps of eastern China, *J. geophys. Res.,* **119**(6), 4802–4820.

Levandowski, W., Jones, C.H., Shen, W., Ritzwoller, M.H. & Schulte-Pelkum, V., 2014. Origins of topography in the western US: mapping crustal and upper mantle density variations using a uniform seismic velocity model, *J. geophys. Res.,* **119**(3), 2375–2396.

Li, H., Su, W., Wang, C.-Y. & Huang, Z., 2009. Ambient noise Rayleigh wave tomography in western Sichuan and eastern Tibet, *Earth planet. Sci. Lett.,* **282,** 201–211.

Li, Y., Wu, Q., Zhang, R., Tian, X. & Zeng, R., 2008. The crust and upper mantle structure beneath Yunnan from joint inversion of receiver functions and Rayleigh wave dispersion data, *Phys. Earth planet. Inter.,* **170**(1), 134–146.

Li, L., Li, A., Shen, Y., Sandvol, E.A., Shi, D., Li, H. & Li, X., 2013a. Shear wave structure in the northeastern Tibetan Plateau from Rayleigh wave tomography, *J. geophys. Res.,* **118**(8), 4170–4183.

Li, Y., Wu, Q., Pan, J., Zhang, F. & Yu, D., 2013b. An upper-mantle S-wave velocity model for East Asia from Rayleigh wave tomography, *Earth planet. Sci. Lett.,* **377,** 367–377.

Lin, F.C. & Ritzwoller, M.H., 2011a. Apparent anisotropy in inhomogeneous isotropic media, *Geophys. J. Int.,* **186**(3), 1205–1219.

Lin, F.-C. & Ritzwoller, M.H., 2011b. Helmholtz surface wave tomography for isotropic and azimuthally anisotropic structure, *Geophys. J. Int.,* **186**(3), 1104–1120.

Lin, F.-C., Moschetti, M.P. & Ritzwoller, M.H., 2008. Surface wave tomography of the western United States from ambient seismic noise: Rayleigh and Love wave phase velocity maps, *Geophys. J. Int.,* **173,** 281–298.

Lin, F.-C., Ritzwoller, M.H. & Snieder, R., 2009. Eikonal Tomography: Surface wave tomography by phase-front tracking across a regional broad-band seismic array, *Geophys. J. Int.,* **177**(3), 1091–1110.

Lin, F.-C., Schmandt, B. & Tsai, V.C., 2012. Joint inversion of Rayleigh wave phase velocity and ellipticity using USArray: Constraining velocity and density structure in the upper crust, *Geophys. Res. Lett.,* **39**(12), doi:10.1029/2012GL052196.

Lin, F.-C., Tsai, V.C. & Schmandt, B., 2014. 3-D crustal structure of the western United States: application of Rayleigh-wave ellipticity extracted from noise cross-correlations, *Geophys. J. Int.,* **198**(2), 656–670.

Liu, J., Han, J. & Fyfe, W.S., 2001. Cenozoic episodic volcanism and continental rifting in northeast China and possible link to Japan Sea development as revealed from K–Ar geochronology, *Tectonophysics,* **339**(3), 385–401.

Luo, Y., Xu, Y. & Yang, Y., 2012. Crustal structure beneath the Dabie orogenic belt from ambient noise tomography, *Earth planet. Sci. Lett.,* **313–314,** 12–22.

Moschetti, M.P., Ritzwoller, M.H., Lin, F.C. & Yang, Y., 2010. Crustal shear velocity structure of the western US inferred from amient noise and earthquake data, *J. geophys. Res.,* **115,** B10306, doi:10.1029/2010JB007448.

Mosegaard, K. & Tarantola, A., 1995. Monte Carlo sampling of solutions to inverse problems, *J. geophys. Res.,* **100**(B7), 12 431–12 447.

Niu, F. & Li, J., 2011. Component azimuths of the CEArray stations estimated from P-wave particle motion, *Earthq. Sci.,* **24**(1), 3–13.

Obrebski, M., Allen, R.M., Zhang, F., Pan, J., Wu, Q. & Hung, S.-H., 2012. Shear wave tomography of China using joint inversion of body and surface wave constraints, *J. geophys. Res.,* **117**(B1), doi:10.1029/2011JB008349.

Rapine, R., Tilmann, F., West, M., Ni., J. & Rodgers, A., 2003. Crustal strucure of northern and sourthern Tibet from surface wave dispersion analysis, *J. geophys. Res.,* **108**(B2), doi:10.1029/2001JB000445.

Ritzwoller, M.H. & Levshin, A.L., 1998. Eurasian surface wave tomography: Group velocities, *J. geophys. Res.,* **103,** 4839–4878.

Ritzwoller, M.H., Levshin, A.L., Ratnikova, L.I. & Egorkin, A.A., 1998. Intermediate period group velocity maps across Central Asia, Western China, and parts of the Middle East, *Geophys. J. Int.,* **134,** 315–328.

Ritzwoller, M.H., Lin, F.C. & Shen, W., 2011. Ambient noise tomography with a large seismic array, *C. R. Geosci.,* **343,** 558–570.

Shapiro, N. & Ritzwoller, M., 2002. Monte-Carlo inversion for a global shear-velocity model of the crust and upper mantle, *Geophys. J. Int.,* **151**(1), 88–105.

Shapiro, N.M., Ritzwoller, M.H., Molnar, P. & Levin, V., 2004. Thinning and flow of Tibetan crust constrained by seismic anisotropy, *Science,* **305,** 233–236.

Shen, W. & Ritzwoller, M.H., 2016. Crustal and uppermost mantle structure beneath the United States, *J. geophys. Res.,* doi:10.1002/2016JB012887.

Shen, W., Ritzwoller, M.H., Schulte-Pelkum, V. & Lin, F.-C., 2013a. Joint inversion of surface wave dispersion and receiver functions: a Bayesian Monte-Carlo approach, *Geophys. J. Int.,* **192**(2), 807–836.

Shen, W., Ritzwoller, M.H. & Schulte-Pelkum, V., 2013b. A 3-D model of the crust and uppermost mantle beneath the Central and Western US by joint inversion of receiver functions and surface wave dispersion, *J. geophys. Res.,* **118**(1), 262–276.

Sun, X., Song, X., Zheng, S., Yang, Y. & Ritzwoller, M., 2013. Three dimensional shear velocity structure of the crust and upper mantle beneath China from ambient noise surface wave tomography, *Earthq. Sci.,* **23,** 449–463.

Tang, Y., Chen, Y.J., Zhou, S., Ning, J. & Ding, Z., 2013. Lithosphere structure and thickness beneath the North China Craton from joint inversion of ambient noise and surface wave tomography, *J. geophys. Res.,* **118**(5), 2333–2346.

Tang, Y., Obayashi, M., Niu, F., Grand, S.P., Chen, Y. J., Kawakatsu, H. & Ni, J.F., 2014. Changbaishan volcanism in northeast China linked to subduction-induced mantle upwelling, *Nat. Geosci.,* **7**(6), 470–475.

Tian, Z.Y., Han, P. & Xu, K.D., 1992. The Mesozoic-Cenozoic East China rift system, *Tectonophysics,* **208**(1–3), 341–363.

Trabant, C., Hutko, A.R., Bahavar, M., Karstens, R., Ahern, T. & Aster, R., 2012. Data products at the IRIS DMC: stepping-stones for research and other application, *Seismol. Res. Lett.,* **83**(6), 846–854.

Villasenor, A., Ritzwoller, M.H., Levshin, A.L., Barmin, M.P., Engdahl, E.R., Spakman, W. & Trampert, J., 2001. Shear velocity structure of Central Eurasia from inversion of surface wave velocities, *Phys. Earth planet. Inter.,* **123**(2–4), 169–184.

Wang, W., Wu, J., Fang, L., Lai, G., Yang, T. & Cai, Y., 2014. S wave velocity structure in southwest China from surface wave tomography and receiver functions, *J. geophys. Res.,* **119**(2), 1061–1078

Xie, J., Ritzwoller, M.H., Shen, W., Yang, Y., Zheng, Y. & Zhou, L., 2013. Crustal radial anisotropy across Eastern Tibet and the Western Yangtze Craton, *J. geophys. Res.,* **118**(8), 4226–4252.

Yang, Y. *et al.*, 2010. Rayleigh wave phase velocity maps of Tibet and the surrounding regions from ambient seismic noise tomography, *Geochem. Geophys. Geosyst.,* **11**(8), Q08010, doi:10.1029/2010GC003119.

Yang, Y., Ritzwoller, M.H., Zheng, Y., Shen, W., Levshin, A.L. & Xie, Z., 2012. A synoptic view of the distribution and connectivity of the mid-crustal low velocity zone beneath Tibet, *J. geophys. Res.,* **117**(B4), B04303, doi:10.1029/2011JB008810.

Yao, H., van Der Hilst, R.D. & Maarten, V., 2006. Surface-wave array tomography in SE Tibet from ambient seismic noise and two-station analysis—I. Phase velocity maps, *Geophys. J. Int.,* **166**(2), 732–744.

Yao, H., Beghein, C. & van der Hist, R.D., 2008. Surface wave array tomography in SE Tibet from ambient seismic noise and two-station analysis: II. Crustal and upper-mantle structure, *Geophys. J. Int.,* **163,** 205–219.

Yao, H., van der Hilst, R.D. & Montagner, J.-P., 2010. Heterogeneity and anisotropy of the lithosphere of SE Tibet from surfacee wave array tomography, *J. geophys. Res.,* **115,** B12307, doi:10.1029/2009JB007142.

Zeng, X. & Ni, S., 2010. A persistent localized microseismic source near the Kyushu Island, Japan, *Geophys. Res. Lett.,* **37,** L24307, doi:10.1029/2010GL045774.

Zeng, X. & Ni, S., 2011. Correction to “A persistent localized microseismic source near the Kyushu Island, Japan”, *Geophys. Res. Lett.,* **38,** L16320, doi:10.1029/2011GL048822.

Zhang, X., Teng, J., Sun, R., Romanelli, F., Zhang, Z. & Panza, G.F., 2014. Structural model of the lithosphere–asthenosphere system beneath the Qinghai–Tibet Plateau and its adjacent areas, *Tectonophysics,* **634,** 208–226.

Zheng, S., Sun, X., Song, X., Yang, Y. & Ritzwoller, M.H., 2008. Surface wave tomography of China from ambient seismic noise correlation, *Geochem. Geophys. Geosyst.,* **9,** Q0502, doi:10.1029/2008GC001981.

Zheng, X.F., Yao, Z.X., Liang, J.H. & Zheng, J., 2010a. The role played and opportunities provided by IGP DMC of China National Seismic Network in Wenchuan earthquake disaster relief and researches, *Bull. seism. Soc. Am.,* **100**(5B), 2866–2872.

Zheng, Y., Yang, Y., Ritzwoller, M. H., Zheng, X., Xiong, X. & Li, Z., 2010b. Crustal structure of the northeastern Tibetan plateau, the Ordos block and the Sichuan basin from ambient noise tomography, *Earthq. Sci.,* **23**(5), 465–476.

Zheng, Y., Shen, W., Zhou, L., Yang, Y., Xie, Z. & Ritzwoller, M.H., 2011. Crust and uppermost mantle beneath the North China Craton, northeastern China, and the Sea of Japan from ambient noise tomography, *J. geophys. Res.,* **116,** B12312, doi:10.1029/2011JB008637.

Zhou, L., Xie, J., Shen, W., Zheng, Y., Yang, Y., Shi, H. & Ritzwoller, M.H., 2012. The structure of the crust and uppermost mantle beneath South China from ambient noise and earthquake tomography, *Geophys. J. Int.,* **189,** 1565–1583.